



Alain Prais Nevière Coimbra

**Reynolds-Averaged Navier-Stokes Modelling of
A Turbulent Lean Premixed Combustor**

Dissertação de Mestrado

Dissertation presented to the Programa de Pós-graduação em Engenharia Mecânica PUC-Rio in partial fulfillment of the requirements for the degree of Mestre em Engenharia Mecânica.

Advisor: Prof. Luís Fernando Figueira da Silva

Rio de Janeiro
September 2019



Alain Prais Nevière Coimbra

**Reynolds-Averaged Navier-Stokes Modelling of
A Turbulent Lean Premixed Combustor**

Dissertation presented to the Programa de Pós-graduação em Engenharia Mecânica PUC-Rio in partial fulfillment of the requirements for the degree of Mestre em Engenharia Mecânica. Approved by the Examination Committee.

Prof. Luís Fernando Figueira da Silva

Advisor

Departamento de Engenharia Mecânica – PUC-Rio

Dr. Valéry Morgenthaler

Ansys – France

Profa. Angela O. Nieckele

Departamento de Engenharia Mecânica – PUC-Rio

Rio de Janeiro, September the 19th, 2019

All rights reserved.

Alain Prais Nevière Coimbra

Graduated in Mechanical Engineering at PONTIFÍCIA UNIVERSIDADE CATÓLICA - RIO DE JANEIRO (Rio de Janeiro, Brazil). Master student at PUC-Rio at the Mechanical Engineering Department in the area of thermal sciences.

Bibliographic data

Prais Nevière Coimbra, Alain

Reynolds-Averaged Navier-Stokes Modelling of A Turbulent Lean Premixed Combustor / Alain Prais Nevière Coimbra; advisor: Luís Fernando Figueira da Silva. – Rio de Janeiro: PUC-Rio, Departamento de Engenharia Mecânica, 2019.

v., 77 f: il. color. ; 30 cm

Dissertação (mestrado) - Pontifícia Universidade Católica do Rio de Janeiro, Departamento de Engenharia Mecânica.

Inclui bibliografia

1. Engenharia Mecânica – Teses. 2. Combustão pré-misturada;. 3. Combustão turbulenta;. 4. Escoamentos com rotação;. 5. Estudo numérico;. I. Figueira da Silva, Luís Fernando. II. Pontifícia Universidade Católica do Rio de Janeiro. Departamento de Engenharia Mecânica. III. Título.

CDD: 620.11

Acknowledgments

I would like to thank professor Luís Fernando for his expert advise and encouragement throughout this project.

My heart also stays with my family, Julie, Miriam and Sergio, for their wise counsel and sympathetic ear. You are always there for me.

I am grateful to Gabriela, Letícia, Nicole, Ricardo and my other colleagues and friends for their wonderful collaboration at the lab. You supported me greatly and were always willing to help me.

Finally, I would like to thank my friends, for providing happy distraction to rest my mind outside of my research.

The authors are also grateful to Dr. Valéry Morgenthaler (Ansys/France) for the assistance and helpful comments on this work. This study was financed in part by the Coordenação de Aperfeiçoamento de Pessoal de Nível Superior - Brasil (CAPES) - Finance Code 001.

Abstract

Prais Nevière Coimbra, Alain; Figueira da Silva, Luís Fernando (Advisor). **Reynolds-Averaged Navier-Stokes Modeling of A Turbulent Lean Premixed Combustor**. Rio de Janeiro, 2019. 77p. Dissertação de mestrado – Departamento de Engenharia Mecânica, Pontifícia Universidade Católica do Rio de Janeiro.

Lean premixed turbulent swirling flames are found in many engineering systems, such as gas turbines and jet engines. This work aims to numerically study flame regimes, representative of such systems, stabilized in a laboratory scale burner. The state of the art of the numerical studies concerning these types of flames is reviewed, with respect to Reynolds-Averaged Navier-Stokes and Large Eddy Simulations. A turbulent, isothermal flow study is performed within the radial swirler and the combustion chamber. The impact of different turbulence models (realizable $k - \epsilon$, RNG $k - \epsilon$ and SST $k - \omega$), mesh refinement levels and boundary conditions on the swirl number and overall flow structure is investigated. The results show that the three tested turbulence models yield similar results, with respect to the obtained flow field, whereas the mesh refinement level and slip wall boundary condition alter the swirl number significantly. Using Reynolds-Averaged Navier-Stokes transport equations, closed by the realizable $k - \epsilon$ model, coupled with a two-equation premixed combustion model for methane/air mixtures, two combustion regimes are analyzed. These regimes correspond to the outer recirculation zone flame (M-shaped flame) and an unstable regime, which occurs at the transition between the V-shaped flame and tornado-flame. The flow structure is characterized in terms of velocity fields, turbulence and combustion properties. A reaction progress variable comparison is also performed, using existing experimental results, yielding qualitatively similar results for both studied regimes.

Keywords

Premixed combustion; Turbulent combustion; Swirling flows; Numerical study;

Resumo

Prais Nevière Coimbra, Alain; Figueira da Silva, Luís Fernando. **Modelagem RANS de uma Câmara de Combustão Turbulenta Pré-misturada**. Rio de Janeiro, 2019. 77p. Dissertação de Mestrado – Departamento de Engenharia Mecânica, Pontifícia Universidade Católica do Rio de Janeiro.

Chamas pré-misturadas em escoamentos turbulentos com rotação são encontradas em diversos sistemas de engenharia, como turbinas a gás e motores a jato. Neste trabalho, regimes de chamas característicos de tais sistemas são estudados numericamente num queimador de escala laboratorial. O estado da arte dos estudos numéricos de tais chamas é revisado, com respeito a simulações de grandes escalas, bem como o de modelos computacionais baseados em médias de Reynolds. Um estudo isotérmico é feito no escoamento turbulento, num domínio computacional que consiste de um swirler radial e uma câmara de combustão. O impacto de diferentes modelos de turbulência, níveis de refinamentos de malha e condições de contorno no número de swirl e na estrutura do escoamento é investigado. Os resultados revelam que os três modelos de turbulência propostos resultam em campos de escoamento e número de swirl similares, enquanto o nível de refinamento de malha e a condição de contorno de parede deslizante alteram o número de swirl significativamente. Utilizando as equações de média de Reynolds, com o fechamento do modelo $k - \epsilon$ realizável, acoplado a um modelo de duas equações para chamas pré-misturadas de metano e ar, dois regimes de chamas são analisados. Estes regimes correspondem à chama de recirculação externa (chama tipo “M”) e um regime de instabilidade, que ocorre na transição entre a chama tipo “V” e chama tornado. A estrutura do escoamento é caracterizada em termos de velocidade e propriedades de turbulência e combustão. Uma comparação entre variáveis de progresso também é feita, utilizando resultados experimentais prévios, levando a boa concordância qualitativa para os dois regimes estudados.

Palavras-chave

Combustão pré-misturada; Combustão turbulenta; Escoamentos com rotação; Estudo numérico;

Table of contents

1	Introduction	13
1.1	Objectives	17
1.2	Manuscript Organization	18
2	Literature Review	19
2.1	Lean Premixed Combustor experimental studies	19
2.2	State-of-the-art - RANS	21
2.3	State-of-the-art – Large Eddy Simulation	24
2.4	State-of-the-Art summary	26
3	Numerical Methodology	28
3.1	Studied experimental configuration	28
3.2	Geometry and computational domain	28
3.3	Model description	31
3.3.1	Turbulence modelling	32
3.3.2	Premixed combustion modelling	34
3.3.3	Adiabatic combustion temperature and laminar flame speed	39
3.4	Mesh generation and boundary conditions	41
3.5	Numerical schemes adopted	43
4	Results and Discussion	44
4.1	Numerical swirl number	44
4.2	Isothermal flow results	53
4.3	Reactive flow results	57
4.3.1	Flame regime IV: Outer Recirculation Zone flame (M-flame)	58
4.3.1.1	Overall flow structure	59
4.3.1.2	Comparison with experimental results	62
4.3.2	Flame regime II: Instability region	64
4.3.2.1	Overall flow structure	64
4.3.2.2	Comparison with experimental results	67
4.4	Borghini diagram analysis	68
5	Conclusion and Perspectives	70
	Bibliography	72

List of figures

Figure 1.1	Open cycle gas turbine configuration. Adapted from (2).	13
Figure 1.2	General electrical (GE) aero-derivative LM6000 lean-premixed (top) and conventional (non-premixed) combustion systems (bottom). Adapted from (7).	15
Figure 1.3	Flow structure illustration induced by a swirling injector. Adapted from (9)	15
Figure 1.4	Burner assembly (left) damaged by combustion instability and new burner assembly (right). Adapted from (10).	16
Figure 2.1	Velocity fields and superimposed Abel-transformed chemiluminescence images, for different equivalence ratios. These correspond to Flames I, III and IV, respectively, as defined by (14). The equivalence ratio for each case is $\phi = 0.52, 0.56$ and 0.66 , respectively.	20
Figure 2.2	Swirler (left): 1 – Fuel/air mixture inlet orifices, 2 – flow outlet area, 3 – bluff body. Combustion chamber: 1 – swirler, 2 – cooling base, 3 – confinement, 4 – quartz window. Adapted from (12).	20
Figure 2.3	Combustion regime diagram, for regime boundaries. Geometrical swirl number $S = 0.4$. Adapted from (13).	21
Figure 2.4	Flow evolution and axial velocity contours for various swirl numbers. Adapted from (19).	23
Figure 3.1	Schematic representation of the experimental setup. Adapted from (13).	29
Figure 3.2	Swirler and corresponding sections.	29
Figure 3.3	Combustion chamber schematic view.	31
Figure 3.4	Schematic view of the computational domain (blue) with superimposed pathlines (black). The anchored flame surface is also displayed (red), represented by a progress variable iso-surface $c = 0.5$ (stoichiometric mixture).	31
Figure 3.5	Simplified Borghi diagram for turbulent premixed combustion. Adapted from (43).	35
Figure 3.6	ITNFS efficiency function Γ_K iso-curves given by Eq.(3-18) as a function of the length scale ratio l_t/δ_l and velocity ratio u'/U_l for methane/air mixtures. Solid lines: $\delta_l = \delta_l^0$, dashed lines: $\delta_l = \delta_l^0 \cdot 2$.	40
Figure 3.7	Adiabatic combustion temperature, as a function of the methane/air mixture equivalence ratio.	41
Figure 3.8	Laminar flame speed (blue), as a function of the methane/air mixture equivalence ratio. A 3rd order polynomial interpolation is also superimposed. Red squares denote experimental results, for comparison purposes (53).	41

- Figure 3.9 Detail of computational mesh in the swirler region (left) and lower part of the combustion chamber (right). Regions with nearly homogeneous distribution of cell sizing are distinguished with roman numbers. 42
- Figure 4.1 Internal region of the swirler (blue), with superimposed pathlines, demonstrating the swirling motion (black). The arrows indicate the flow orientation. The swirler exit surface in which the swirl number is calculated is highlighted (red). 44
- Figure 4.2 Detail of swirler exit section. From left to right: meshes 1, 2 and 3. 46
- Figure 4.3 Contours of z velocity component at the planar section of the swirler, from inlet (bottom) to outlet (top) for 6 different cases, as described in Tab.4.1. 48
- Figure 4.4 Contours of turbulent viscosity ratio in the planar section of the swirler, for 3 different meshing cases, a , b and c . 49
- Figure 4.5 Contours of y velocity component at the planar section of the swirler, with detail on the top (exit) part. Two types of boundary conditions are compared: no slip walls (case b , left) and walls with zero shear stress (case f , right). 49
- Figure 4.6 Contours of absolute pressure in the planar section of the swirler, with detail on the top (exit) part. Such as Fig. 4.5, cases of no slip walls (case b , left) and walls with zero shear stress (case f , right) are compared. 50
- Figure 4.7 Contours of y velocity component (top) and tangential velocity component (bottom) for cases b and f , at the swirler exit surface, highlighted in Fig. 4.1. 51
- Figure 4.8 Circumferentially averaged values of y velocity component (dashed lines) and tangential velocity component (solid lines) at the exit surface, for cases b (blue) and f (red), as a function of the radius. 52
- Figure 4.9 Contours of wall y^+ at the external walls with inlet orifices (left) and internal walls (right) of the swirler for case b . 53
- Figure 4.10 Representation of recirculation bubbles, through iso-surfaces of $v_y = 0$ m/s (blue), with superimposed streamlines from the swirler exit (black), for isothermal cases a , b and c , summarized in Tab. 4.2. 55
- Figure 4.11 Contours of y velocity component at the planar section of the lower combustion chamber region for cases a , b and c , summarized in Tab. 4.2. 56
- Figure 4.12 Contours of x velocity component (top), turbulent viscosity ratio (middle) and turbulent kinetic energy (bottom), at the planar section of the lower combustion chamber region for cases a , b and c , summarized in Tab. 4.2. 57
- Figure 4.13 Representation of recirculation bubbles, through iso-surfaces of $v_y = 0$ m/s (blue), with superimposed streamlines from the swirler exit (black) (left) and contours of vertical velocity component, v_y , at the combustion chamber section (right). 60

Figure 4.14	Contours of vertical velocity for heights $y = 0, 10, 20, 30$ and 40 mm, from the combustion chamber base.	60
Figure 4.15	Contours of flow and combustion properties. (a): vertical velocity; (b): horizontal velocity; (c): temperature field at the ORZ; (d): turbulent viscosity ratio at the swirling jet and ORZ; (e): Damköhler number at the swirling jet and ORZ; (f): flame surface density (Σ).	62
Figure 4.16	Flame regime IV: contours of computed progress variable (left) and average OH radical binarized image, measured with PLIF (right), adapted from (13).	63
Figure 4.17	Flame regime IV: contours of computed progress variable using the Zimont Turbulent Flame Closure model (left) and average OH radical binarized image, measured with PLIF (right), adapted from (13).	64
Figure 4.18	Representation of recirculation bubbles, through iso-surfaces of $v_y = 0$ m/s (blue), with superimposed streamlines from the swirler exit (black) (left) and contours of vertical velocity component, v_y , at the combustion chamber section (right).	65
Figure 4.19	Contours of vertical velocity for heights $y = 0, 10, 20, 30$ and 40 mm, from the combustion chamber base.	66
Figure 4.20	Contours of flow and combustion properties. (a): vertical velocity; (b): horizontal velocity; (c): temperature field at the ORZ; (d): turbulent viscosity ratio at the swirling jet and ORZ; (e): Damköhler number at the swirling jet and ORZ; (f): flame surface density (Σ).	67
Figure 4.21	Flame regime II: contours of computed progress variable (left) and average OH radical binarized image, measured with PLIF (right), adapted from (13).	68
Figure 4.22	Simplified Borghi diagram for turbulent premixed combustion. Adapted from (43). The computed flame regimes locations at the diagram are given by the ellipses.	69

List of tables

Table 4.1	Studied cases for isothermal swirl number.	45
Table 4.2	Isothermal studied cases of turbulence modelling influence.	54

List of Abbreviations

ARC – Analytically Reduced Chemistry
BC – Boundary Conditions
CFD – Computational Fluid Dynamics
CRZ – Central Recirculation Zone
DES – Detached Eddy Simulation
DNS – Direct Numerical Simulation
ECFM – Extended Coherent Flamelet model
EDM – Eddy Dissipation Model
ER – Equivalence Ratio
IRZ – Inner Recirculation Zone
ITNFS – Intermittent Turbulent Net Flame Stretch
LES – Large Eddy Simulation
LPC – Lean-Premixed Combustor
OH-PLIF – Hydroxyl radical Planar Laser-Induced Fluorescence
ORZ – Outer Recirculation Zone
RANS – Reynolds-Averaged Navier-Stokes
RNG – Renormalization Group theory
SAS – Scale Adaptive Simulation
TI – Thermoacoustic Instability

1 Introduction

Gas turbines are continuous combustion engines, consisting mainly of three components: an upstream gas compressor, downstream turbine, and combustion chamber, as schematized in Fig. 1.1. Their basic operation may be described in a Brayton cycle (1), using air as a working fluid. The external fresh atmospheric air is pressurized by flowing through the compressor. At the combustion chamber, energy is added to the system, through the injection of fuel and ignition of the resulting mixture. The expansion of the high-pressure, high-temperature combustion products through the turbine produces shaft work. The resulting jet flow may be directly used as thrust power in turbojet engines, or may drive secondary rotating components for other types of power generation.

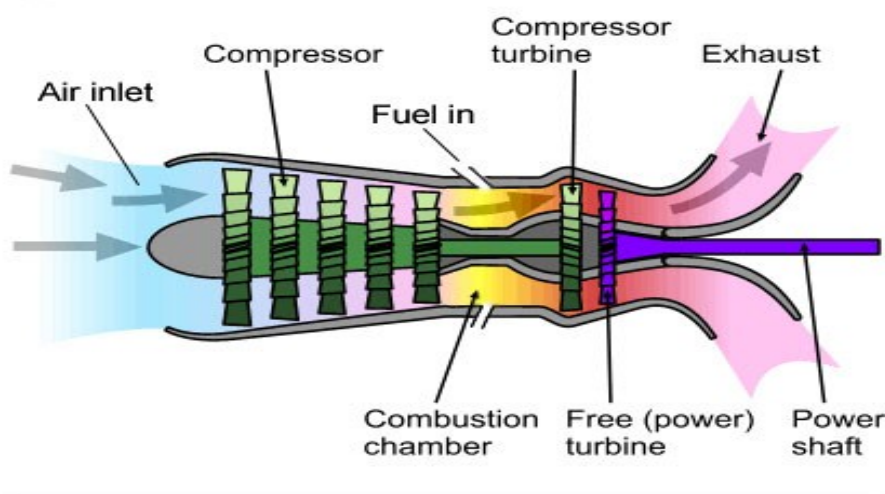


Figure 1.1: Open cycle gas turbine configuration. Adapted from (2).

The gas turbine high power-to-weight ratio, if compared to reciprocating engines, makes them an attractive option for aircraft propulsion. Since the heat released by the combustion process is transferred almost entirely to the exhaust stream, it may be used effectively for boiling water or for co-generation purposes, also. Gas turbines are also an interesting option for large scale energy production systems, such as electrical generators, due to the high efficiency of the associated combined cycle systems.

As will be seen in chapter 2, several experimental and numerical studies of the reactive flow in combustion chambers representative of gas turbines have been conducted in the past decades. The major aim of these studies has been to investigate efficiency, stability and noise reduction. These design parameters are often related to the mixing of fuel and air in the combustion chamber or pre-chamber, flow characteristics, turbulence control and chamber geometry, for instance.

Classically, gas turbines have often relied on combustion chambers with diffusion flames, due to their reliability and acceptable efficiency (3). Most often liquid fuel is sprayed directly into the chamber, and ignition occurs without complete pre-mixing of fuel and air. This results in higher burning temperature at locations where combustion is close to a stoichiometric proportion. Emissions of nitrogen oxides (NO_x) are high at these burning temperatures (4), which has become prohibitive due to the modern emissions regulations in most countries.

Reduction of such pollutant emissions has been a major thrust on the development of modern combustion devices. A promising configuration adopted for the combustion chamber of modern gas turbines is that of turbulent lean premixed swirling flames (5). The lean premixing of reactants leads to lower burning temperatures, which significantly diminishes the emissions of NO_x, as well as formation of soot. The capability of burning the mixture at lower fuel/air equivalence ratios also implies in fuel economy. In these configurations, the swirler, a mechanical device that induces a significant amount of tangential momentum to the flow, imposes a turbulent, swirling flow, which aids in the flame stabilization. However, perfect pre-mixing must be ensured before ignition. This work is devoted to the investigation and understanding of such combustion systems, as well as to a numerical study regarding turbulent lean premixed, swirl-stabilized premixed combustion.

An example of a lean-premixed turbine combustor practical configuration, in comparison to a conventional diffusion flame system, is given in Fig. 1.2. The former employs a triple annular design for fuel staging to achieve an ultra-lean flame with a reduced temperature. Double annular counter-rotating swirler premix injectors are adopted, necessary for generating the swirling motion in the reacting flow. The conventional system consists of a single annular combustor, in which gaseous fuel is directly injected. A more detailed description of these two combustion systems may be found in (6), (7) and (8).

A scheme of a typical fundamental configuration adopted in experimental studies is depicted in Fig. 1.3. As it may be seen, pre-mixing of fuel and air occurs upstream to the flame holder. After a sudden expansion at the swirler

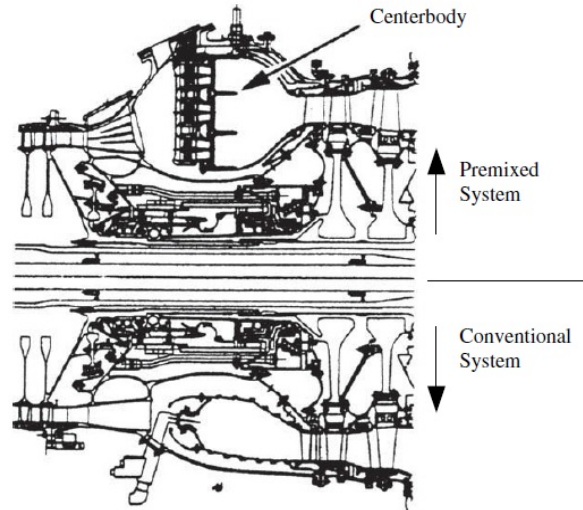


Figure 1.2: General electrical (GE) aero-derivative LM6000 lean-premixed (top) and conventional (non-premixed) combustion systems (bottom). Adapted from (7).

exit, ignition occurs within the chamber. The stabilized flow is confined by the chamber walls, consisting of quartz windows that allows for the anchored flame visualization.

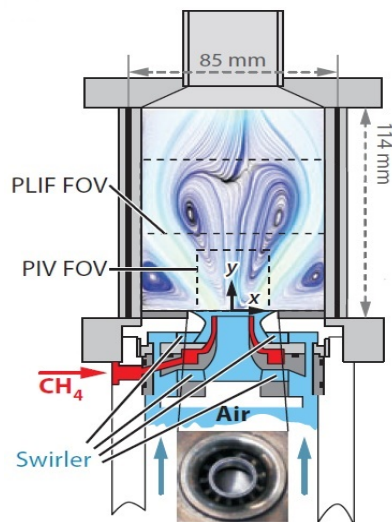


Figure 1.3: Flow structure illustration induced by a swirling injector. Adapted from (9)

Several flame macrostructures may be observed in this configuration. These topologies are a consequence of multiple parameters, such as equivalence ratio, swirl number, volumetric flow rate, combustion chamber geometry, fuel composition, among others. The resulting flame may also interact with the chamber walls, penetrate recirculation zones or even uncouple from the swirler.

Appropriate denominations and descriptions of each observed topology are addressed in the next section.

In such lean premixed configurations, it is imperative to understand how the different combustor parameters affect the flow field, turbulence, and combustion properties, in order to avoid the occurrence of unstable combustion. This phenomenon, also known as thermoacoustic instability (TI), may arise from interactions between pressure fluctuations and combustion heat release oscillations (9), and is characterized by intense flame flickering and oscillation. Unstable behavior may be perceived in a variety of ways, from minor noise discomfort to high levels of sound pressure with destructive capabilities, which can be lethal in cases of aircraft engines malfunction (10). Fig. 1.4 shows a burner assembly damaged by such instabilities, in comparison to a new burner assembly designed to avoid these occurrences.



Figure 1.4: Burner assembly (left) damaged by combustion instability and new burner assembly (right). Adapted from (10).

The phenomenon of thermoacoustic instabilities has received significant attention, as modern measurement tools and computational resources have allowed a better understanding of its causes and unsteady characteristics. State of the art numerical and experimental works in the field of lean-premixed turbulent, swirling flows are also presented and discussed in this work.

Thermoacoustic instabilities that occur from transitions between two stable regimes may be detected experimentally as a function of specific parameters, such as fuel composition, equivalence ratio and volumetric flow rate. Several recent studies are devoted to the categorization of these parameters, such as those performed at Combustion and Turbulence Laboratory at PUC-Rio (11), (12) and (13). Indeed, different swirlers, with different swirl numbers, have been considered, in order to generate a controlled flow in a squared-sectioned combustion chamber. This work is devoted to the numerical investigation of

the lean-premixed combustor (LPC) configuration studied experimentally at PUC-Rio. The overarching goal of this joint effort is to understand the parameters that lead to stable combustion and its characteristics.

It is of special interest here to obtain an increased knowledge of the flow field, turbulence properties and combustion characteristics of radial swirler and combustion chamber. Different flame macrostructures are to be defined and described, as a function of methane/air equivalence ratio and total volumetric flow rate across the domain. To achieve these goals, a computational fluid dynamics (CFD) finite volume technique is employed.

An isothermal flow characterization in the combustion chamber must be first performed. Isothermal studies, which are considerably faster and computationally cheaper than reactive models, allow to understand the flow characteristics and to address turbulence modelling choices. Furthermore, mesh verification is simpler to perform in such isothermal flow fields. Turbulence modelling choices are also briefly discussed. Premixed combustion and turbulence models interactions are then coupled to the isothermal flow field. The study of the reactive flow mechanics is explained, and modelling choices are also discussed. Flame macrostructures are obtained for different controlled equivalence ratios of the methane/air mixture. Comparison with experimental results are finally drawn.

1.1 Objectives

The main objective of this work is to present the results of a numerical study regarding lean-premixed swirling combustor. To achieve this goal, it is proposed to:

- Identify the state of the art numerical and experimental studies regarding turbulent, swirling lean-premixed combustors;
- Perform an isothermal flow study, for mesh verification, turbulence model choice influence and boundary condition determination;
- Perform the reactive flow study, in order to characterize the flow field and identify flame topologies;
- Compare regimes limits and characteristics with the corresponding experimental results;

1.2

Manuscript Organization

This work is organized in five sections:

1. Introduction: motivation and objectives;
2. Literature Review: description of the experimental counterpart of this work, as well as other similar experimental lean premixed combustion studies. State-of-the-art numerical studies regarding lean premixed combustion are also presented, with respect to Large Eddy Simulations and Reynolds-Averaged Navier-Stokes modelling.
3. Numerical methodology: A brief description of the experimental configuration is performed, as well as of turbulence and premixed combustion modelling. The methodology for computational domain generation, solving and boundary conditions is given;
4. Results and Discussion: Results of the identified flame topologies are presented. Comparisons with experimental studies are drawn, in terms of limits for regimes transitions;
5. Conclusions and Perspectives: The conclusions and perspectives for future works are discussed;

2

Literature Review

In this chapter the experimental configuration that motivates this work is first discussed, as well as relevant experiments regarding lean premixed swirling combustors, in which flow characteristics and flame topologies are clearly described. An overview of state-of-the-art numerical studies is presented, regarding both Large Eddy Simulations (LES) and Reynolds-Averaged Navier-Stokes (RANS) turbulent flow simulations. Also in this last section, the state-of-the-art experimental studies are briefly discussed.

2.1

Lean Premixed Combustor experimental studies

A literature review indicates that several lean premixed swirling combustors experiments have recently been addressed, such as described in this chapter. Different combustion regimes and instability characteristics have been observed in turbulent methane/hydrogen/air flames in a swirling flow, as depicted in Fig. 2.1 (14). This figure represents the averaged streamlines on which Abel-transformed chemiluminescence images have been superimposed, representing the time-averaged location of the flame surface. The fuel/air mixture enters the combustion chamber from the swirler, which is coupled at its bottom, directed upwards. Due to the sudden expansion, the mixture strongly interacts with the chamber walls. An outer recirculation zone (ORZ) can be seen at the corners of the chamber, represented by a flow redirection towards the bottom. Both the expansion and swirling motion also generate an inner recirculation zone (IRZ).

Figure 2.1 shows that, at the lowest equivalence ratio (ER), the flame stabilizes inside the IRZ (Flame I). If the ER is further reduced, the flame detaches from the swirler, and eventually extinguishes. On the other hand, as the ER is increased, the flame stabilizes in the inner shear layer (ISL), which is the jet comprised between the IRZ and ORZ. In this situation, the flame strongly interacts with the chamber walls (Flame III). At the largest ER value, the flame anchors at the ORZ (Flame IV) also. It has been shown that the critical equivalence ratio for the transition of these topologies changes as hydrogen is added to the methane/air mixture.

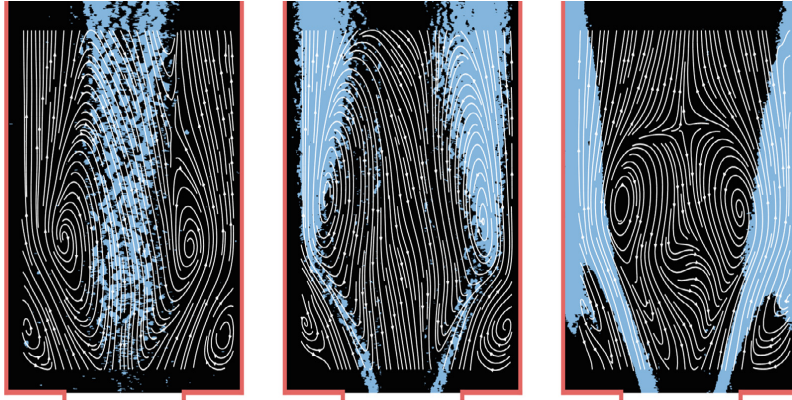


Figure 2.1: Velocity fields and superimposed Abel-transformed chemiluminescence images, for different equivalence ratios. These correspond to Flames I, III and IV, respectively, as defined by (14). The equivalence ratio for each case is $\phi = 0.52, 0.56$ and 0.66 , respectively.

An experimental analysis of flame topologies in swirl-stabilized flows has also been carried out (15). Transitions between topologies and their interactions with the combustion chamber walls have been discussed, as parameters controlling the shape of swirling flames were identified. Therefore, by identifying the key physical mechanisms and the appropriate dimensionless numbers controlling topological transitions, the parameters that needs to be explored could be reduced to critical Karlovitz and Lewis numbers.

The numerical studies presented in this work are the counterpart to the experimental research activities performed at PUC-Rio, which uses a novel premixed turbulent swirling combustion test bench. The swirler and combustion chamber used in such experiments are presented in Fig. 2.2.

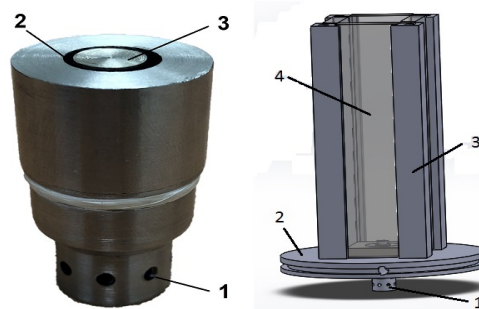


Figure 2.2: Swirler (left): 1 – Fuel/air mixture inlet orifices, 2 – flow outlet area, 3 – bluff body. Combustion chamber: 1 – swirler, 2 – cooling base, 3 – confinement, 4 – quartz window. Adapted from (12).

Using two different swirlers and, therefore two different swirl numbers, several flame topologies for methane/air combustion have been observed (11),

for the confined and unconfined situations. Blow-off limits for both swirlers have also been determined, in terms of equivalence ratio and volumetric flow rate.

Using the same swirler and combustion chamber configurations as (11), stable and unstable regimes have been examined (12). For two values of the geometrical swirl number, OH chemiluminescence allowed visualization of different flame topologies, also as a function of methane/air equivalence ratio and volumetric flow rate. Stability boundaries have been determined, also as a function of these parameters.

Flame topologies have also been analyzed (13) using the OH planar laser-induced fluorescence (PLIF-OH) technique. Three stable regimes – I, III and IV – and one unstable regime – II – have been characterized. The observed flame structures have also been categorized in combustion regime diagrams, as depicted in Fig. 2.3.

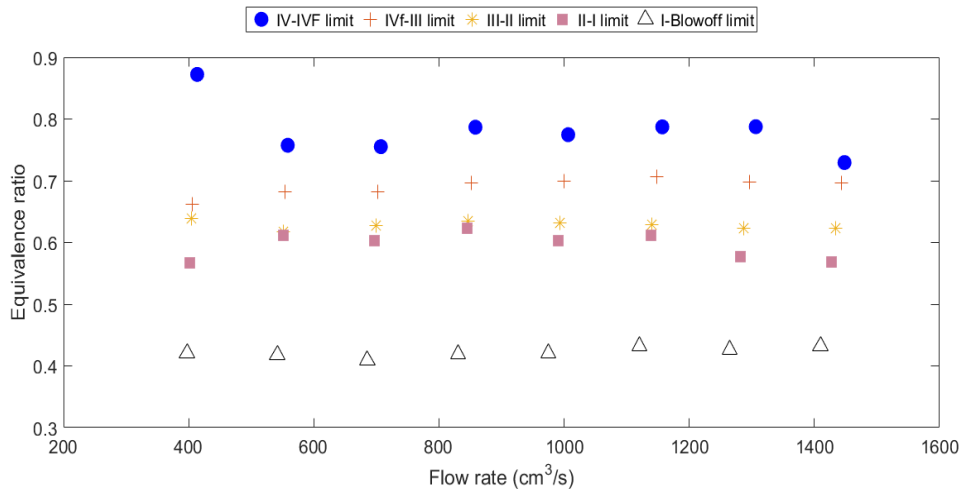


Figure 2.3: Combustion regime diagram, for regime boundaries. Geometrical swirl number $S = 0.4$. Adapted from (13).

2.2

State-of-the-art - RANS

Turbulent flows are dominant in almost all engineering practices. In contrast to laminar flows, they are characterized by a strong nonlinear behavior in pressure and flow velocity fields. Due to its strong chaotic nature, turbulence is often described as the most important unsolved problem in classical physics (16). State-of-the-art numerical studies regarding interactions between turbulence and premixed combustion in swirl-stabilized combustors are discussed in this section.

Numerical simulation of turbulent flows is often classified into three categories: Direct Numerical Simulation (DNS), Large-Eddy Simulation (LES) and Reynolds-Averaged Navier-Stokes (RANS). DNS consists of numerically solving the relevant temporal and spatial flow scales without the use of turbulence models. The associated computational cost is very high, even at low Reynolds numbers situations. Therefore, DNS remains viable for simple geometries and flow fields only. LES consists of filtering the smallest length scales from the solution. Since this small scale information is relevant to the description of the flow field, it must be modelled appropriately. In RANS, the effects of the turbulent fluctuations, resulting from the time-averaging of the Navier-Stokes equations, are modelled in order to achieve closure of the equation system. This approach is frequently used for engineering applications, due to its reasonable computational cost.

The state-of-the-art of Reynolds-Averaged Navier-Stokes simulation studies pertaining to lean premixed combustion in gas turbines is now addressed, based on a literature review (17). Advantages of lean-premixed combustors have been explained, as well as its difficulties and challenges. Turbulence modelling, and its interactions with chemical reactions have been discussed in the context of time-averaged Navier-Stokes equations.

That work indicated that turbulence predictions have been mostly carried out using $k - \epsilon$ modelling, though the isotropic nature of its turbulent viscosity does indeed limit the model capabilities for accurately predicting swirling flows. Algorithms for pressure correction have usually relied on the SIMPLE technique.

Accordingly, the most used approaches for turbulent combustion modelling, from least to most complex, have been determined to be:

1. Laminar chemistry: ignores the effect of turbulent fluctuations in the reacting flow;
2. Eddy dissipation model (EDM): relates the reaction rate with gross turbulent properties. The reaction rate is usually assumed to be proportional to the inverse of the turbulent time scale;
3. Assumed-shape PDF method: uses a turbulent fluctuation PDF to estimate the influence on the reaction rate;
4. Scalar PDF methods: treat complex, finite-rate chemistry without assuming a PDF;

Most common practices for methane/air combustion includes two and four-step mechanisms for the prediction of CO emissions, and five or nine-

step mechanisms for NO. These mechanisms have been often derived from the detailed, 276-step, 49 species, GRI-Mech 2.11 mechanism (18).

A RANS approach regarding swirl effects on the flame dynamics of a lean premixed combustor has also been recently addressed (19). Three turbulence closure models have been tested - Standart $k - \epsilon$, Realizable $k - \epsilon$ and SST $k - \omega$. The turbulence-chemistry interaction is addressed with Finite Rate-Eddy Dissipation model, with a three step global reaction mechanism. Flame stability limits have been defined and flow behavior and flame dynamics have been described, as a function of the swirl number. The Realizable $k - \epsilon$ model has been determined to be the most predictive for high swirl numbers, as it has shown best agreement with experimental results. Fig. 2.4 indicates streamlines along the nozzle and combustion chamber for different swirl numbers with axial velocity contours. Arrows indicate the flow orientation. The jet expansion at the nozzle exit generates an outer recirculation zone, which can be perceived at all swirl numbers. For a critical swirl number, around 0.75, an inner recirculation zone, also referred as vortex breakdown, has been found to arise.

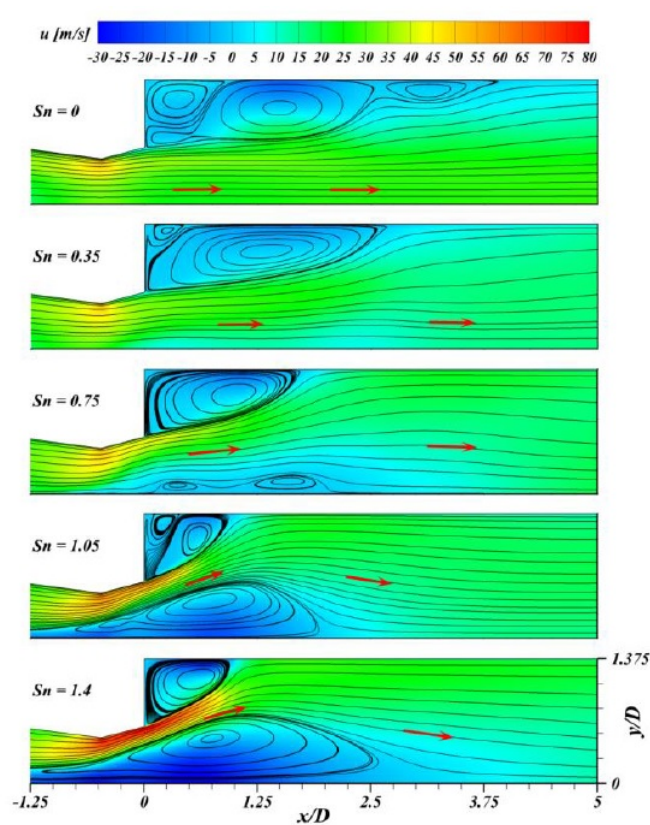


Figure 2.4: Flow evolution and axial velocity contours for various swirl numbers. Adapted from (19).

Using the same configuration for swirler and combustion chamber, a

more detailed and sophisticated approach than RANS has been suggested (20). A study has been conducted using Detached Eddy Simulations (DES) - a modification of RANS in which the model switches to a subgrid scale formulation in regions fine enough for LES calculations (20). This method has been able to predict the reacting flow field in stagnation points and vortices in the inner and outer shear layers, as compared to experimental results. The SST $k - \omega$ turbulence model combined with a finite rate/eddy dissipation model of the reacting DES has been able to predict the fields of averaged axial velocity and average temperature profiles with more precision than the standard RANS.

2.3

State-of-the-art – Large Eddy Simulation

Most recent numerical studies of turbulent, swirling flame dynamics employ large eddy simulations. LES is a particularly attractive approach for the study of unstable regimes, where the flow field of concern is unsteady and dominated by turbulent motions that cannot be adequately resolved using classical Reynolds-Averaged Navier-Stokes models. This section addresses the Large-Eddy Simulation studies regarding instabilities that arise from interactions between pressure fluctuations and combustion heat release oscillations in turbulent, swirling combustors, since these represent the state-of-the-art of lean premixed combustion simulations.

Potential sources that may control the overall quality of LES results for turbulent premixed flames have been recently identified (21). Chemistry description, flame/turbulence interaction modelling, numerical solving, boundary conditions, wall numerical treatments and wall temperature and heat losses have been pointed out as being crucial. The first three among these have been addressed and discussed, and comparisons have also been drawn with experimental results.

An improvement of the chemical scheme accuracy has been proposed: from a two-step scheme of fast oxidation of propane and air and CO – CO₂ equilibrium to an Analytically Reduced Chemistry (ARC) consisting of 22 species. Similar studies (22) have also shown that this improvement could be directly related to a better representation of the flame response to stretch. Regarding flame/turbulence interactions on the sub grid scale, a dynamic Thickened Flame (TFLES) model has been proposed, in place of a static TFLES model. Flame fronts are usually too thin to be resolved on LES grids, and modelling is required to handle this fundamental difficulty. TFLES consists of artificially thickening the flame's spatial structure to allow its resolution on the numerical grid (23). Furthermore, the dynamic TFLES approach

automatically estimates correction coefficient terms, from the resolved progress variable field, and a user-adjustable model constant is no longer required. The order of accuracy of the numerical method has been shown to play a significant role in order to capture the growth rates of hydrodynamic instabilities along the flame front. A higher, third-order scheme for spatial discretization was shown to yield better results than a lower, second-order scheme, and it is necessary in order to accurately capture the flame response to stretch.

On a partially premixed swirling combustor, large eddy simulations have been conducted in order to investigate the mixing of fuel and air in the swirler and burner nozzle that leads to thermoacoustic oscillations (24). Using a Scale Adaptive Simulation (SAS) technique for the modelling of turbulent fluctuations, the efficiency of two combustion models - Eddy Dissipation Model (EDM) and a detailed Finite Rate Chemistry Model (FRC) - has been investigated and compared with experimental results. The EDM utilizes a two-step mechanism, whereas the FRC models the methane/air combustion reactions with a skeletal scheme consisting of 19 species. While both schemes have been proved to acceptably reproduce the available experimental results of velocity, temperature and mixture fraction, the FRC model led to a better prediction of the flame lift-off height. This demonstrates an improved representation of the strong unsteady turbulence-chemistry interactions, which occur near the flame base.

Numerical studies of a premixed swirling burner have also been performed (25). Using the TFLES model, global and local dynamic formulations for the flame wrinkling factor are compared. A correction factor has been introduced for the flame wrinkling in the flame/wall interaction. Global constants for the static model exponent have also been defined. Self-excited modes of the pulsating flame have been captured by using this dynamic mode.

The importance of thermal boundary conditions on the combustor walls for the prediction of instability regimes has also been identified as a relevant issue (26). As classified in that work, state-of-the-art LES of combustors employ four types of wall boundary conditions:

1. Adiabatic walls;
2. Prescribed wall temperatures;
3. Prescribed local heat flux;
4. Conjugate heat transfer at the combustor walls.

Modelling of the burner solid structure has been found out to not contribute to significant changes on the mean velocity field, but to improve the prediction of

frequency and amplitude of unstable modes, when compared to experimental results.

Along with Large Eddy Simulations, recent experimental studies have also been conducted in order to improve the understanding of the operating conditions that lead to thermoacoustic instabilities. The behavior and interaction of two flames has been studied in a sequential combustor (27). The first flame is described as a classical, perfectly-premixed swirl stabilized flame, whereas the second one exhibits different combustion modes depending on the local mixture temperature and composition. Using OH-PLIF, OH chemiluminescence and acoustic pressure measurement techniques, interactions between acoustic pressure and heat release fluctuations have been discussed. Good agreement has been obtained with LES results, using analytically reduced chemistry, regarding acoustic mode shape and the oscillatory flame dynamics.

A joint experimental and numerical study has also been conducted (28) regarding a swirl-stabilised cylindrical combustor. Chemiluminescence and dynamic pressure measurements have been used to study thermoacoustic instabilities in a lean premixed methane/air flame. Concerning LES, an Eulerian stochastic field method has been applied to describe turbulence/chemistry interactions. Additionally, through the use of dynamic mode decomposition, unstable flame modes could be investigated, and the azimuthal transport of hot combustion products around the centerline of the combustion chamber analyzed.

Instabilities that arise from mutual interactions between pressure fluctuations and heat release oscillations have also been investigated (29) at a staged combustor with a central pilot flame surrounded by an annular flame. Correlations between flame macrostructures and TI have been described. Three stable flame topologies have been observed as a function of the equivalence ratio and stratification ratio: stratified flame, V-shaped flame and lifted flame.

2.4

State-of-the-Art summary

This literature review has allowed to identify the joint effort of numerical and experimental works regarding lean-premixed combustion in turbulent, swirling flows. Several experimental techniques, such as Particle Image Velocimetry (PIV), OH planar laser-induced fluorescence (PLIF-OH) and OH chemiluminescence have been explored, in order to capture reactive flow characteristics.

Concerning the numerical studies, RANS models still receive attention

due to their reasonable computational cost. However, the unsteady behavior of thermoacoustic instabilities, that usually occurs at transitions between stable regimes, is often studied using LES, which requires more computational power and sophisticated modelling. The main parameters that control quality of LES results have been often identified as chemistry description, flame/turbulence interaction modelling, numerical solving, boundary conditions, wall numerical treatments and wall temperature and heat losses.

This work is thus devoted to the numerical study of a lean-premixed turbulent swirling combustion configuration. To this end, a Reynolds-Averaged Navier-Stokes modelling of a LPC novel combustion chamber, experimentally studied at the Combustion and Turbulence Laboratory at PUC-Rio is performed.

3 Numerical Methodology

In this chapter, the numerical methodology is presented. The studied experimental configuration of the lean premixed burner is first discussed. The domain of interest associated to such configuration is then exposed, and the computational domain meshing procedure is analyzed. A model description of turbulence and combustion is briefly given, boundary conditions details and difficulties are explained, and the numerical schemes given.

3.1 Studied experimental configuration

The lean premixed burner experimental test bench, developed at the Combustion and Turbulence Laboratory at PUC-Rio, consists of a radial swirler and the adjoining square-sectioned combustion chamber, as presented in Fig. 2.2 (13). A scheme of the overall experimental configuration is shown in Fig. 3.1. The obtained flame topology fields that are used for comparison purposes in that work have been measured using the planar laser induced fluorescence technique (30). In that study, a dye laser system and an intensified charge-coupled device camera have been used to analyze the flame regimes. The experimental combustion chamber contains quartz walls, which allows for optical visualization of the flame (13).

The methane and air mixture enters the swirler from six orifices, radially distributed at its base, as it may seen in Fig. 3.2. The orifices are offset with respect to the swirler main body axis, which induces a significant amount of tangential momentum to the flow. The fluid flows upwards in an annular space, between the external wall and an internal cylindrical structure. The bluff body, an inverted cylindrical structure is found at the end of the device, which narrows the flow before exiting the swirler. The mixture finally expands as it flows upwards at the device's exit and into the combustion chamber.

3.2 Geometry and computational domain

The swirler described in this section is denominated SW06I (13). The overall design, inlet and outlet sections are presented in Fig. 3.2. The bluff

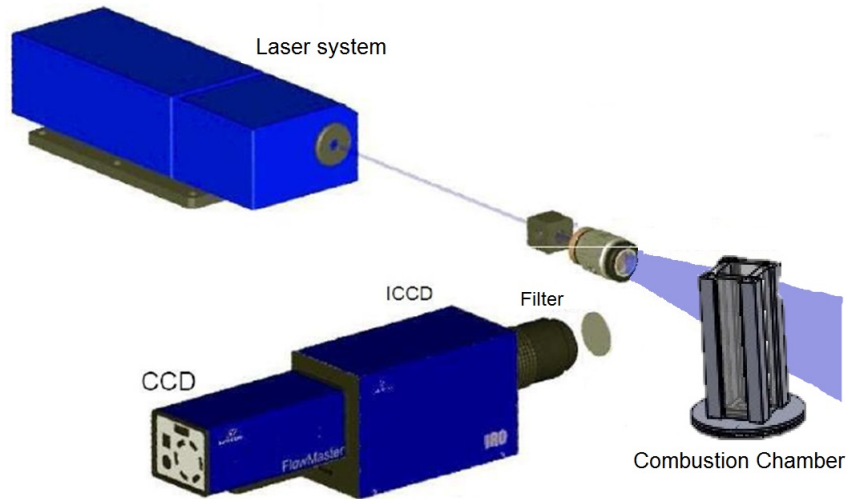


Figure 3.1: Schematic representation of the experimental setup. Adapted from (13).

body main function is to provide for the flame anchoring near the combustion chamber base. It may be seen from Fig. 3.2(a) that the SW06I has the bluff body surface flushed to the surface of the swirler exit. Fig. 3.2(b) shows the swirler inlet section, where it may be observed that the mixture is fed tangentially to the chamber. In this particular swirler, six air/fuel inlets, with identical diameters, are radially distributed at the device's base. The swirler exit section is depicted in Fig. 3.2(c). The inverted cone can be perceived at the upper base, narrowing the flow upstream to the expansion at the combustion chamber. The swirler has a total height of $H = 30$ mm.

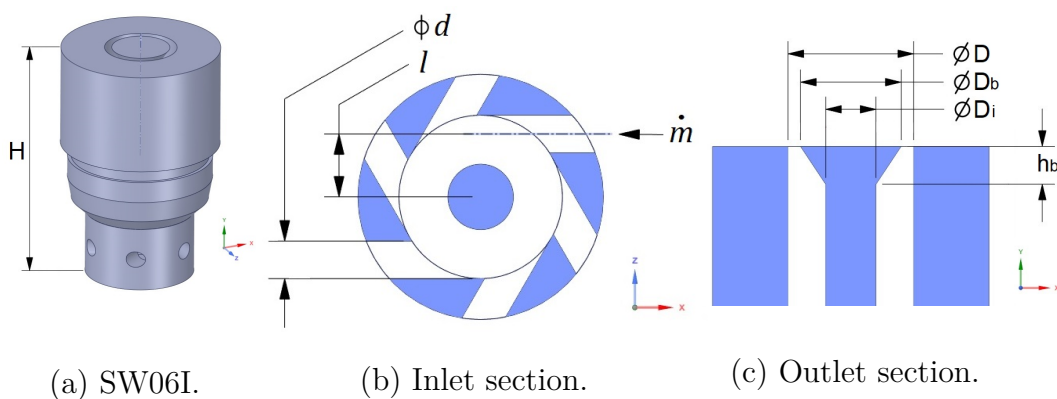


Figure 3.2: Swirler and corresponding sections.

The swirl number is an important parameter for characterizing the intensity of the swirling motion. It is defined by the ratio between the axial flux of tangential momentum, G_θ , and the axial momentum flux, G_z (31):

$$S = \frac{G_\theta}{RG_z} = \frac{\int_0^R u_z u_\theta r^2 dr}{R \int_0^R u_z^2 r dr}, \quad (3-1)$$

where R is the swirler radius. The swirl number of the swirler SW06I has been estimated from its geometrical properties, assuming a solid body rotation flow within the device, a uniform axial velocity and negligible pressure effects (13). The corresponding swirl number may thus written as:

$$S = \frac{lD}{nd^2} \left[1 - \left(\frac{D_b}{D} \right)^2 \right] \approx 0.4, \quad (3-2)$$

where l is the offset distance of the inlet orifice, relative to the main axis, D is the swirler outer diameter, n is the number of orifices, d is the orifice diameter, and D_b is the diameter of the inverted cone base. For the studied swirler SW06I, $l = 3.85$ mm, $D = 10$ mm, $n = 6$, $d = 2.3$ mm and $D_b = 8$ mm.

In this work, the swirl number is also determined numerically at the swirler exit surface, which is delimited between the outer diameter and the inverted cone base. The corresponding values and discrepancies with respect to the geometrical approximation [Eq.(3-2)] are exhibited and discussed in section 4.1.

As shown in Fig. 3.3, the combustion chamber is square-sectioned, with a width of $L = 40$ mm. The actual chamber height at the experimental setup is $H_c = 170$ mm, but it has been reduced to $H_c = 100$ mm in this work due to computational resources limitations. Regimes with long flames, such as Flame I, described in section 2.1, are thus expected to present some differences, as it will be discussed in the results section. A pyramid-shaped convergent structure is placed at the top of the combustion chamber, which provokes a flow acceleration at the domain outlet. The top structure has a height of $H_p = 15$ mm and the outlet has a width of $L_p = 10$ mm. This structure is a modelling artefact which diverges from the experimental counterpart of this work. Indeed, the acceleration of the flow near the domain outlet has proved to prevent the occurrence of reverse flow, which interferes with the converging process of the numerical solution.

For illustration purposes, a general scheme of the whole computational domain is given by Fig. 3.4. As it may be seen, the superimposed pathlines indicate the flow orientation, from the six inlets at the swirler base to the convergent exit at the top of the combustion chamber, as well as a recirculation after the fluid expansion from the swirler exit. A representation of the flame anchored by the swirling flow within the chamber may also be noted through a combustion progress variable iso-surface of $c = 0.5$, as will be discussed in

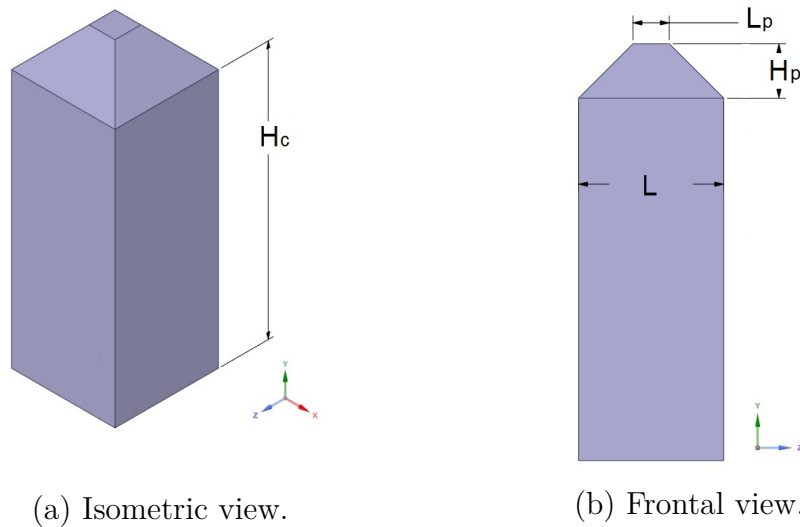


Figure 3.3: Combustion chamber schematic view.

the next section.

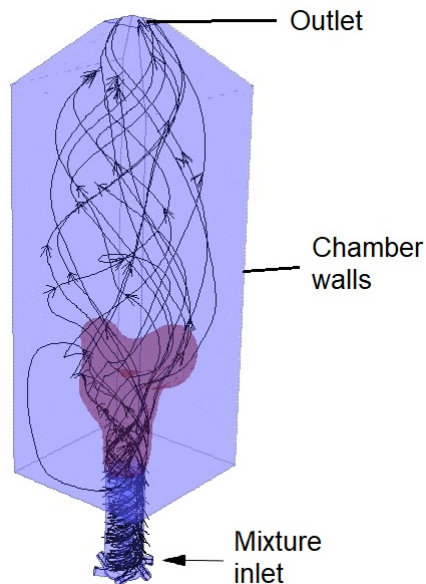


Figure 3.4: Schematic view of the computational domain (blue) with superimposed pathlines (black). The anchored flame surface is also displayed (red), represented by a progress variable iso-surface $c = 0.5$ (stoichiometric mixture).

3.3

Model description

The numerical simulations in this work have been performed using a code from *Ansys/Fluent*. This is motivated by a partnership with *Ansys/France* in the framework of the Magister consortium (32). The physical and chemical models used in this work are directly chosen from this code available choices.

For the sake of brevity, efforts of validation, in terms of the solution procedure, have not been made in this work.

In all studied cases, the balance equations of momentum and mass have been solved together with turbulence and combustion models. The functions and particularities of each model are briefly discussed and their primary sources are referenced, where they have been derived and presented with a more detailed description. First, turbulence model choices are examined, which have been applied to isothermal and reactive flow studies. One-equation and two-equation premixed combustion models are then addressed and compared. Finally, methods for defining premixed flame properties are exposed.

3.3.1

Turbulence modelling

The turbulence closure problem in this work is solved using Reynolds-Averaged Navier-Stokes equations, due to their reasonable computational cost. The models used in this work belong to the class of two-equation models, in which transport equations are solved for two turbulence quantities. From these quantities, lengthscales and timescales may be formed (16).

$k - \epsilon$ model

The $k - \epsilon$ model is a widely used turbulence model and it is found in most commercial CFD codes. It is often described as a robust, economic and reasonably accurate solution for a wide range of industrial flows and heat transfer simulations (33).

In the derivation of the $k - \epsilon$ model, it is assumed that the flow is fully turbulent (corrections for flows with low Reynolds-numbers are therefore required) and the effects of molecular viscosity are negligible. Its first transported property is the turbulent kinetic energy k , which describes the energy of the turbulent fluid motion. The second one is commonly referred to as the turbulent dissipation rate, ϵ , which determines the small scales of the turbulence. The third important specification in the $k - \epsilon$ model is the turbulent viscosity, which, in the standard formulation, is modelled as a function of these transported flow properties using the Boussinesq hypothesis (34):

$$\nu_t = C_\mu \frac{k^2}{\epsilon}, \quad (3-3)$$

where C_μ is a model parameter.

Two variations of the $k - \epsilon$ model have been used in this work: The Realizable and the RNG models. The differences in these new formulations consist, mainly, in the method for calculating the turbulent viscosity, the

turbulent Prandtl numbers, which govern the turbulent diffusion terms in k and ϵ balance equations, and the generation and destruction terms in the ϵ equation.

The RNG $k - \epsilon$ uses a statistical technique, i.e., the renormalization group theory, for the derivation of the associated transport equations (35). Consequently, additional refinement terms may be observed:

- An additional term in the turbulent dissipation equation, which improves the accuracy for rapidly strained flows.
- A correction for the effect of swirl, which enhances accuracy for predicting swirling flows.
- An analytical formula for turbulent Prandtl number, instead of user-specified, constant values.
- The implementation of an analytically-derived differential formula for effective viscosity that allows corrections for low-Reynolds-number flows.

The realizable $k - \epsilon$ consists mainly of a new formulation for the turbulent viscosity. The standard two-equation model is known to be over-predictive for the eddy viscosity in cases of flows with a high mean shear rate, due to its turbulent viscosity formulation. This formulation is improved by ensuring mathematical realizability, involving the effect of mean rotation on turbulence stresses, and avoiding negative normal stresses in cases of large mean strain rates. This model also incorporates a new dissipation rate equation, based on the dynamic equation for fluctuating vorticity. It has been shown to predict more accurately the behaviour of flows involving rotation (36).

$k - \omega$ model

The $k - \omega$ is another common two-equation turbulence model found in CFD codes. The standard model has been shown to predict free shear flow spreading rates that are in close agreement with measurements for mixing layers and plane, round and radial jets, and is thus capable of predicting wall-bounded flows and shear flows (37). The standard $k - \omega$ is an empirical model based on transport equations for the turbulent kinetic energy k , such as the $k - \epsilon$ model, and specific dissipation rate ω , which may be interpreted as being proportional to the ratio of ϵ to k (38). The turbulent viscosity, in the standard formulation, is modelled as a function of these transported flow properties:

$$\nu_t = \alpha^* \frac{k}{\omega}, \quad (3-4)$$

where α^* is a damping coefficient which causes corrections for low Reynolds-number flows.

The shear-stress transport (SST) $k - \omega$ model is a more recent enhancement of the standard model. It is an attempt to blend the formulation of the $k - \omega$ model in the near-wall region with the free-stream independence of the $k - \epsilon$ model in the far field. To achieve this, the following refinements are made regarding the $k - \omega$ and $k - \epsilon$ models:

- Both models are multiplied by a blending function and summed. This function is designed to activate the standard $k - \omega$ model in the near-wall region and the transformed $k - \epsilon$ model in the region away from the surface,
- The SST model incorporates a damped cross-diffusion derivative term in the specific dissipation rate balance equation,
- The turbulent viscosity formula incorporates a term to account for the transport of the turbulent shear stress,
- The modelling constants are adapted.

These refinements have been shown to allow to enhance the $k - \omega$ model predictability for a variety of flows, such as airfoils, transonic shock waves and adverse pressure gradient flows (39).

3.3.2

Premixed combustion modelling

The combustor studied in this work belongs to the group of premixed combustion devices. A perfectly homogeneous methane and air mixture is thus assumed to enter the computational domain, with a known fuel/air equivalence ratio. The turbulence/combustion interaction problem is discussed in this section. Two choices of classical premixed combustion models are considered: a one-equation and a two-equation model.

Premixed turbulent combustion regimes

A diagram typically used for classifying premixed turbulent combustion regimes, in terms of velocity and length scales ratios, is illustrated in Fig. 3.5. The behaviour of the flames obtained with the two premixed combustion models, with respect to their location on this diagram, is illustrated and discussed in section 4.4. The y axis represents a ratio between the characteristic turbulent velocity fluctuation, u' , and the laminar flame speed, U_l , a property of homogeneous combustible mixtures, which is studied in section 3.3.3. The x axis represents a ratio between an integral turbulent length scale, l_t and the flame thickness, δ_l (40).

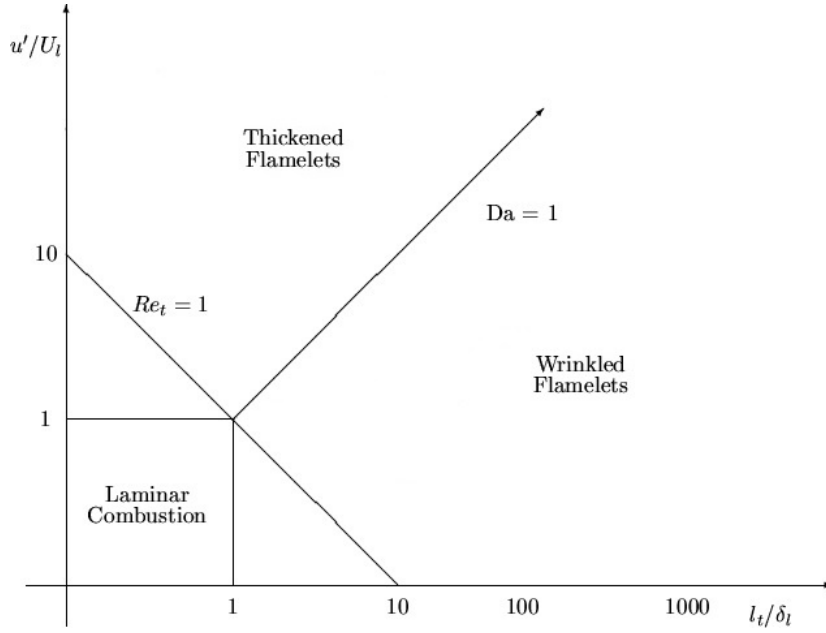


Figure 3.5: Simplified Borghi diagram for turbulent premixed combustion. Adapted from (43).

From the two-equation RANS models treated in this work, described in section 3.3.1, the root-mean-square velocity fluctuation is determined by

$$u' = \sqrt{2k/3}, \quad (3-5)$$

directly from the transport of turbulent kinetic energy, k , upstream to the flame brush.

The integral turbulence length scale is determined as (16)

$$l_t = C_D \frac{(u')^3}{\epsilon}, \quad (3-6)$$

where C_D is a model parameter, with a value of $C_D = 0.37$, and ϵ is the transported turbulence dissipation rate (41), taken upstream of the flame brush also.

The flame thickness is estimated as (42)

$$\delta_l = 2 \left(\frac{T_b}{T_u} \right)^{0.7} \frac{\alpha}{U_l}, \quad (3-7)$$

where T_u and T_b denote the unburnt and burnt temperatures, which account for a correction due to the expansion of the gas. The local unburnt mixture thermal diffusivity is α , with a used value of $\alpha = 10^{-5} \text{ m}^2/\text{s}$, which corresponds to the methane/air mixture at a temperature of $T_u = 300 \text{ K}$. Note that

a value of thermal diffusivity for nitrogen gas at ambient temperature is $\alpha_{N_2} \approx 2 \cdot 10^{-5} \text{ m}^2/\text{s}$.

From these velocity and length scales, the turbulent Reynolds number is defined as

$$Re_t = \frac{u' l_t}{U_l \delta_l}, \quad (3-8)$$

which gives the relative importance of turbulent and molecular transport, whereas the turbulent Damköhler number is

$$Da = \frac{U_l l_t}{u' \delta_l}, \quad (3-9)$$

which compares an integral turbulence time scale upstream to the flame to a characteristic chemical time scale of the heat release process (40).

As a consequence of Eqs.(3-8) and (3-9), and since a log-log representation is used in Fig. 3.5, lines of constant Re_t exhibit a -45° derivative, whereas a constant Da line has a 45° one. Thus, as it may be seen in Fig. 3.5, the area below the unity turbulent Reynolds line represents a region where combustion occurs in a laminar flow. This area is, naturally, of little interest to the modelling of turbulence/combustion interactions. Flame regimes located below the $Da = 1$ line and for $Re_t > 1$ are denoted as wrinkled flamelets. In these premixed flames, the flame time scale is smaller than the smallest turbulence time scales, also known as the Kolmogorov eddies. As a consequence, the effect of turbulence is to wrinkle the flame sheet. The chemical reaction and the internal flame structure should remain unaltered from the laminar case. This assumption has been used on the formulation of all premixed combustion models used in this work.

Zimont turbulent flame closure model

The first model that has been adopted in this work involves the solution of a transport equation that accounts for the turbulent premixed combustion: the reaction progress variable. In this formulation, a one-step, irreversible chemical reaction between fresh gases and combustion products is considered (44). The progress variable c is a binary entity, where $c = 0$ denotes fresh gases and $c = 1$ denotes burnt gases. This variable has been introduced, and its consequences to modelling analysed by Bray, Moss and Libby(45). The progress variable is usually interpreted as a normalized temperature:

$$c = \frac{T - T_u}{T_b - T_u}. \quad (3-10)$$

The usual additional assumptions for the numerical model formulation simplification are: perfect gases, incompressible flow, constant heat capacities and unity Lewis numbers. This model has been derived to describe a flame in the wrinkled flamelets region, discussed in the previous section.

The unclosed transport equation of the progress variable, c , has the form:

$$\frac{\partial}{\partial t} (\bar{\rho}\tilde{c}) + \frac{\partial}{\partial x_i} (\bar{\rho}\tilde{u}_i\tilde{c}) = \frac{\partial}{\partial x_i} \left(\bar{\rho} \frac{\nu_t}{Sc_c} \frac{\partial \tilde{c}}{\partial x_i} \right) + \bar{w}_c. \quad (3-11)$$

Both time-based (Reynolds) and density-based (Favre) averages have been used, denoted as $(\overline{\cdot\cdot\cdot})$ and $(\tilde{\cdot\cdot\cdot})$, respectively (16). The first term on the RHS of the equation is a closure of turbulent scalar fluxes, known as the gradient assumption, and it is often used in turbulent combustion models (46), even if it may be of questionable validity for flames with large expansion ratios between the fresh and burnt gases (47). The turbulent viscosity, ν_t , is estimated from the turbulence model, as detailed in section 3.3.1. The turbulent Schmidt number defines the ratio of the turbulent transport of momentum and the turbulent transport of mass and it is assumed to have a constant value of $Sc_c = 0.7$ (41).

The average chemical source term, \bar{w}_c , is treated with the turbulent flame speed closure, proposed by Zimont (48), i.e.,

$$\bar{w}_c = \rho_u U_t \left| \frac{\partial \tilde{c}}{\partial x_i} \right|, \quad (3-12)$$

where ρ_u is the density of the unburnt mixture, and U_t is the turbulent flame velocity normal to the mean flame surface. The value of U_t is influenced by the following:

- The laminar flame speed, which is a property determined as a function of the fuel concentration, temperature, molecular diffusion properties and chemical kinetics, and is calculated in section 3.3.3.
- The effect of turbulence on the flame front, such as the flame surface wrinkling and stretching by large eddies, and flame thickening by small eddies.

This allows the turbulent flame speed to be computed with (48):

$$\frac{U_t}{U_l} = ADa^n \left(\frac{u'}{U_l} \right), \quad (3-13)$$

where A and n are model constants, of value $A = 0.52$ and $n = 1/4$. The closure equation used in this work is an expansion form of Eq.(3-13), and it is also a function of the integral turbulent length scale, l_t , defined in Eq.(3-6):

$$U_t = A u'^{(3/4)} U_l^{(1/2)} \alpha^{(-1/4)} l_t^{(1/4)}. \quad (3-14)$$

Numerical results using this model are presented in section 4.3. Model validation, via comparisons with experimental results, as well as alternative approaches may be found in the literature (49).

Extended Coherent Flamelet model

The Extended Coherent Flamelet model (ECFM) is a refinement of classical models for the reactive scalar \tilde{c} . This model uses an additional equation for the flame surface density, which is used as a more physically realistic way of predicting the chemical rate term in Eq.(3-11). One advantage of this approach is to separate the finite rate chemistry influence, incorporated into the average flame speed $\langle s_c \rangle$, from turbulence/combustion interactions modelled by the flame surface density Σ (50). The mean reaction rate becomes, then:

$$\bar{w}_c = \rho_u \langle s_c \rangle \Sigma. \quad (3-15)$$

In the formulation used in this work, the effects of strain in the mean flamelet consumption speed, $\langle s_c \rangle$, are neglected, and it is assumed to be the laminar flame speed: $\langle s_c \rangle \equiv U_l$.

This model assumes, also, that the studied flame is located at the wrinkled flamelets region on the Borghi diagram, illustrated in Fig. 3.5. The equation for the transport of the net flame surface area per unit volume Σ may be written as:

$$\frac{\partial}{\partial t} (\Sigma) + \frac{\partial}{\partial x_i} (\tilde{u}_i \Sigma) = \frac{\partial}{\partial x_i} \left(\frac{\nu_t}{Sc_c} \frac{\partial \Sigma}{\partial x_i} \right) + \kappa_t \Sigma - D, \quad (3-16)$$

where κ_t and D are unclosed terms which require, therefore, modelling. The turbulent strain rate, κ_t , is related to the stretch rate of the flame due to the turbulence motions, and D is a destruction term required to avoid the infinite growth of the flame surface area (51).

The turbulent strain rate is estimated by the Intermittent Turbulent Net Flame Stretch (ITNFS) technique as a function of a turbulent time scale ϵ/k and an efficiency parameter Γ_K available in the Fluent code, which is a function of the flame/turbulence interaction quantities detailed in the previous section:

$$\kappa_t = \alpha_0 \Gamma_K \left(\frac{u'}{\bar{U}_l}, \frac{l_t}{\delta_l} \right) \frac{\epsilon}{k}, \quad (3-17)$$

where α_0 is a constant, $\alpha_0 = 1.6$, and Γ_K has been fitted from DNS data as (52):

$$\log_{10}(\Gamma_K) = -\frac{1}{(s+0.4)} \exp[-(s+0.4)] + \{1 - \exp[-(s+0.4)]\} \left[\sigma_1 \left(\frac{u'}{U_l} \right) s - 0.11 \right], \quad (3-18)$$

where

$$s = \log_{10} \left(\frac{l_t}{\delta_l} \right) \quad \text{and} \quad \sigma_1 \left(\frac{u'}{U_l} \right) = \frac{2}{3} \left[1 - \frac{1}{2} \exp \left(- \left(\frac{u'}{U_l} \right)^{1/3} \right) \right]. \quad (3-19)$$

The flame area destruction term is modelled in this work as:

$$D = \beta U_l \frac{\Sigma^2}{1 - \tilde{c}}, \quad (3-20)$$

where β is a constant with the value of one.

The ITNFS treatment accounts for the reduced ability of small vortices to wrinkle the flame front. Since the used expression for the flame thickness, Eq.(3-7), is the result of order of magnitude analysis, assessing the influence of δ_l on Γ_K may lead to some insights on the model behaviour. Accordingly, this is affected by arbitrarily multiplying δ_l by a factor of 2 in Eq.(3-19). This leads to a smaller s value and, thus, influences Γ_K . An analysis of Fig. 3.6 allows to verify Γ_K behaviour on the Borghi diagram. The efficiency function value increases as the length scale ratio l_t/δ_l increases. For a given l_t/δ_l , this modification result in a smaller Γ_K value, which in turn, is expected to decrease the flame surface creation terms, via Eq.(3-17). It may be also perceived in this figure that Γ_K only slightly depends on the velocity ratio u'/U_l .

3.3.3

Adiabatic combustion temperature and laminar flame speed

The adiabatic combustion temperature is the equilibrium value from a complete combustion process that occurs without any work, heat transfer or changes in kinetic or potential energy in the system (42). It is a necessary information for determining the temperature field in the system:

$$T = (1 - c)T_u + c T_b, \quad (3-21)$$

where T_u is the temperature of the unburnt mixture and T_b is the adiabatic combustion temperature.

The adiabatic combustion temperature and laminar flame speed, which has been discussed in the previous section, have been numerically determined for methane/air combustion. For different equivalence ratios ϕ , ranging from

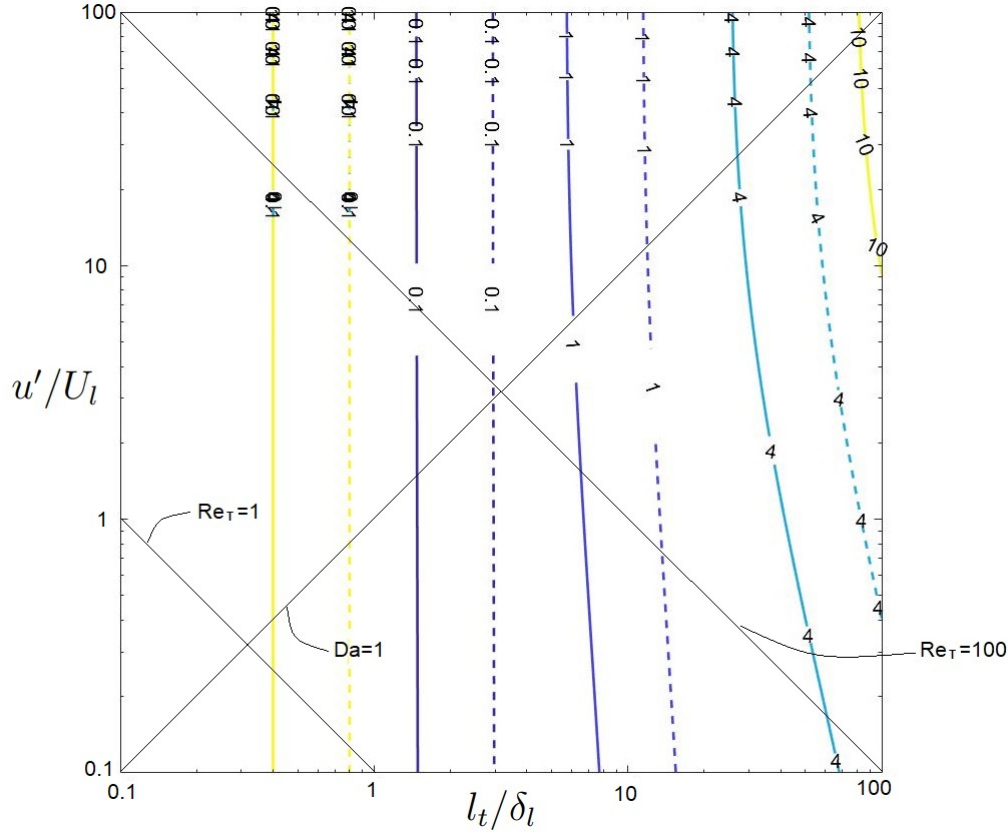


Figure 3.6: ITNFS efficiency function Γ_K iso-curves given by Eq.(3-18) as a function of the length scale ratio l_t/δ_l and velocity ratio u'/U_l for methane/air mixtures. Solid lines: $\delta_l = \delta_l^0$, dashed lines: $\delta_l = \delta_l^0 \cdot 2$.

$\phi = 0.4$ to $\phi = 1.0$ at atmospheric conditions, the obtained values are given in Fig. 3.7 and Fig. 3.8. As it may be observed, good agreement is obtained with experimental results for the laminar flame speed (53).

These numerical simulations have been carried out with the CHEMKIN-PRO code, using the GRIMECH 3.0 mechanism for kinetics, thermodynamics and transport properties of the involved species (54). This classical mechanism consists of 53 species and 325 reactions. For the computation of the adiabatic flame temperature and the laminar flame speeds, the equilibrium and premixed flame speed models have been used, respectively.

The obtained values of T_b are applied in Eq.(3-7), and values of U_l are used in Eqs. (3-7), (3-8), (3-9), (3-13), (3-14), (3-17) and (3-20). The laminar flame speed is mainly used as a metric in the combustion/turbulence interaction study and for determination of the turbulent flame speed, as discussed in the previous section.

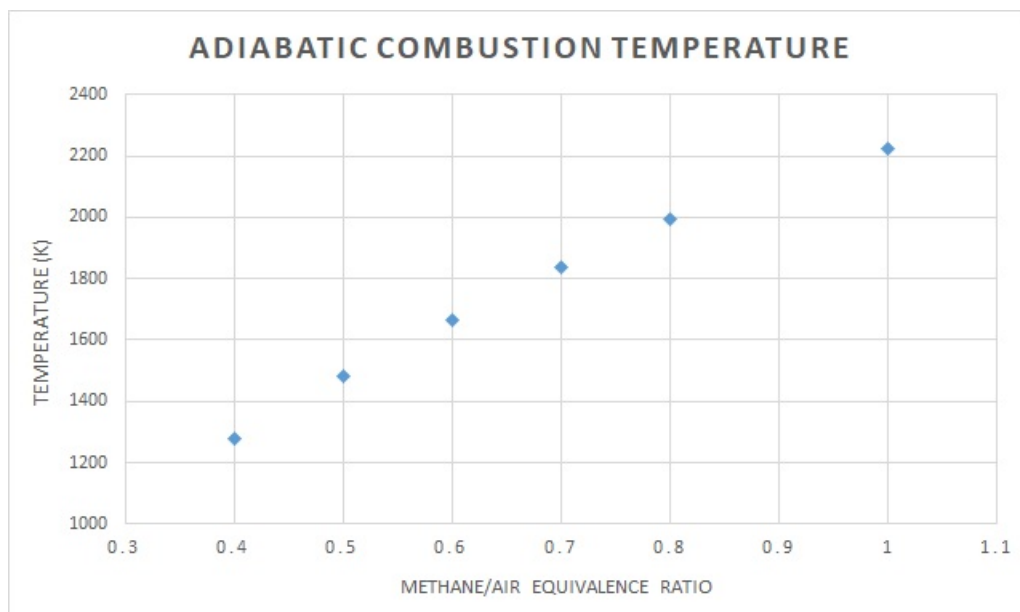


Figure 3.7: Adiabatic combustion temperature, as a function of the methane/air mixture equivalence ratio.

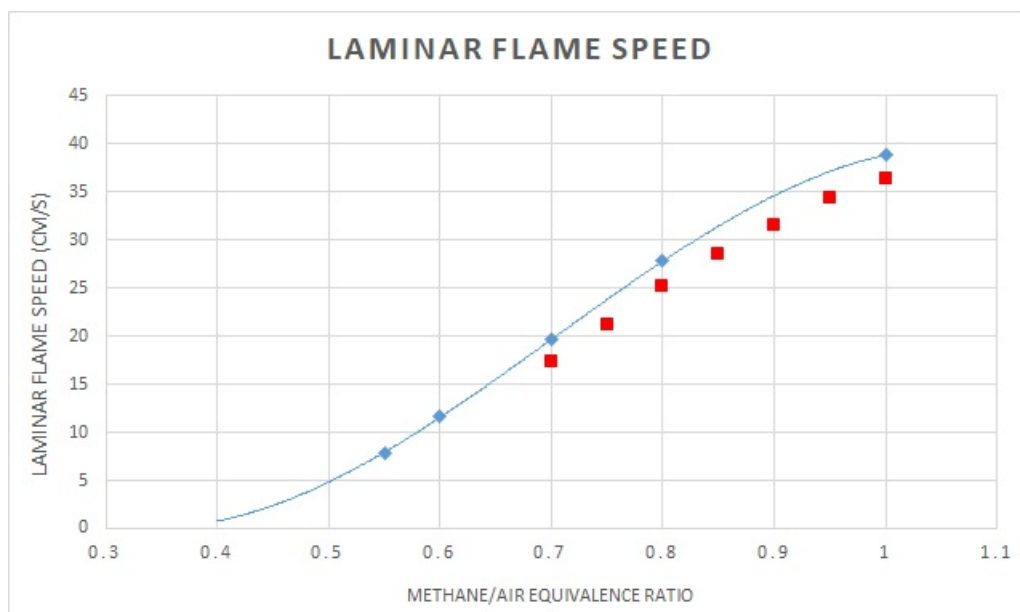


Figure 3.8: Laminar flame speed (blue), as a function of the methane/air mixture equivalence ratio. A 3rd order polynomial interpolation is also superimposed. Red squares denote experimental results, for comparison purposes (53).

3.4 Mesh generation and boundary conditions

The computational grid has been obtained in this work using the software *Fluent Meshing* from *Ansys*. A three-dimensional mesh is generated from the computational domain described in the previous section. All meshings in this

work consist of unstructured polyhedral elements.

The characteristic length of the grid is defined in this work as the cubic root of the mean volume of the cells in a specific region of the mesh:

$$\Delta = V^{1/3}, \quad (3-22)$$

where V is the mean volume of a cell in a region of the mesh with homogeneous cell distribution. This property is discussed in chapter 4.

The computational grid is refined at the swirler's surface and lower combustion chamber regions, where larger gradients of velocity, turbulence and combustion properties are expected to occur. Only one element is placed normal to the wall surfaces throughout the domain, with length of $\Delta = 0.035$ mm on the smallest cells, which are located around the inverted cone base. The assumptions and consequences of this decision are discussed in section 4.1.

The overall computational grid applied in this domain is illustrated in Fig. 3.9. This section is perpendicular to the combustion chamber base and lateral windows, and crosses the swirler at the center of the bluff-body. Regions with different mean cell sizes are identified by roman numbers. The characteristic length of each region is $\Delta_I = 0.30$ mm, $\Delta_{II} = 0.10$ mm, $\Delta_{III} = 0.23$ mm and $\Delta_{IV} = 1.00$ mm. The study of the influence of the mesh refinement in the swirler section in the flow field is performed in section 4.1. This mesh consists of approximately 3.4 million elements, and is used in the isothermal and reactive flow simulations in sections 4.2 and 4.3, respectively.

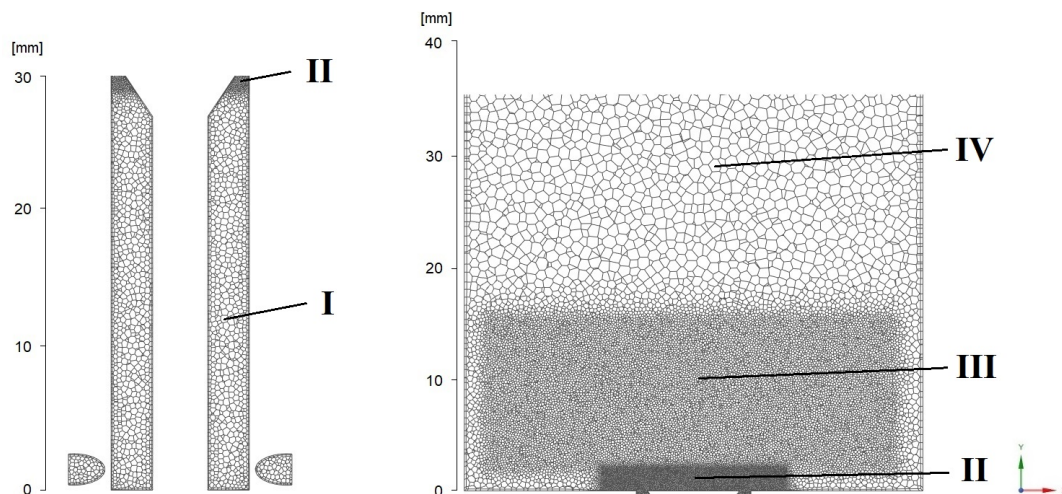


Figure 3.9: Detail of computational mesh in the swirler region (left) and lower part of the combustion chamber (right). Regions with nearly homogeneous distribution of cell sizing are distinguished with roman numbers.

The six inlets at the base of the swirler are set as pressure inlet boundary conditions (BC). A fixed absolute pressure of $P_{in} = 101$ kPa is set in all inlet surfaces, illustrated in Fig. 3.2. The outlet is the reduced area at the top of the combustion chamber, resulted from the usage of the pyramid-shaped structure, depicted in Fig. 3.3. This area has been designed to equal the total surface area of the six inlet surfaces, which is a technique for avoiding the occurrence of reverse flow at the outlet boundaries. A constant mass flow rate BC is set at the outlet surface, directed outwards, relative to the computational domain. All walls have no slip and adiabatic conditions, i.e., zero heat exchange with the exterior, unless otherwise stated. All turbulence models use standard wall functions for near-wall treatment.

3.5

Numerical schemes adopted

The pressure-based coupled algorithm is used for pressure-velocity coupling. Spatial discretization for momentum, progress variable and flame area density balance equations use the second-order upwind scheme. For the turbulent kinetic energy and turbulent dissipation rate equation, the first-order upwind scheme is used. Both steady and transient RANS are used in this work. All relaxation factors are set as default, according to Ansys Fluent 2019 R1. The first-order implicit scheme is used for the transient formulation, with a time-step of $\Delta_t = 2 \cdot 10^{-5}$ s, which respects the limits for the cell convective Courant number.

Residual monitoring uses a $R = 10^{-5}$ tolerance value. For some properties, residuals have converged at values above this threshold, as will be briefly discussed at the isothermal and reactive flow studies in the next section.

4 Results and Discussion

In this chapter, the numerical results are presented and discussed. The numerical swirl number is determined and used as a comparison metric for meshing, turbulence modelling and boundary conditions at the swirler walls. Comparisons with the geometrical swirl number presented in section 3.2 are also drawn. The study of the turbulence model choice on the isothermal flow within the combustor is then performed. The reactive results are finally presented, and the corresponding flow field properties are analyzed for different methane/air equivalence ratios and premixed combustion models.

4.1 Numerical swirl number

The numerical swirl number is calculated using Eq.(3-1), and is the ratio between the axial flux of tangential momentum and the axial momentum flux through the swirler exit surface, which is the annular region between the device's outer wall and the inverted cone base, as highlighted in Fig. 4.1.

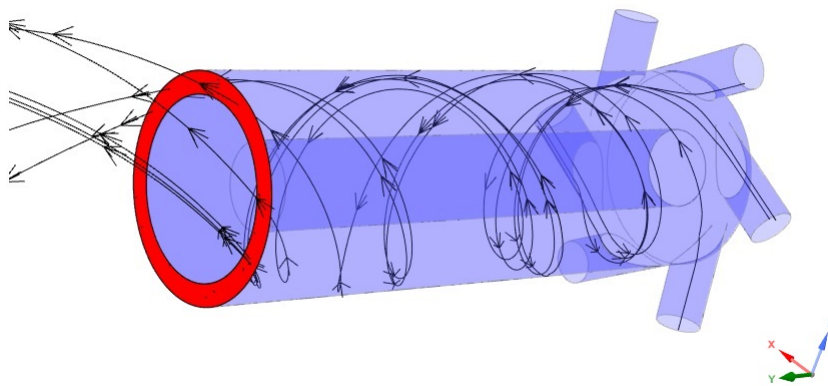


Figure 4.1: Internal region of the swirler (blue), with superimposed pathlines, demonstrating the swirling motion (black). The arrows indicate the flow orientation. The swirler exit surface in which the swirl number is calculated is highlighted (red).

The swirl number is determined for different sets of parameters choices, which are summarized in Tab. 4.1. Three meshings of the computational

domain at the swirler region, two distinct boundary conditions for the swirler walls and three turbulence models have been considered.

Table 4.1: Studied cases for isothermal swirl number.

Case	Mesh	Turbulence model	Boundary condition	Swirl number
a	1	Realizable $k - \epsilon$	no slip	0.83
b	2	Realizable $k - \epsilon$	no slip	0.75
c	3	Realizable $k - \epsilon$	no slip	0.72
d	2	SST $k - \omega$	no slip	0.77
e	2	RNG $k - \epsilon$	no slip	0.73
f	2	Realizable $k - \epsilon$	slip	1.13

Mesh:

A comparison between meshings may be seen in Fig. 4.2. The depicted section is perpendicular to the combustion chamber base and lateral windows and crosses the swirler at the center of the bluff-body, thus allowing to visualize the swirler exit, as well as the lower and central part of the combustion chamber.

- Mesh 1: A coarser mesh, consisting of approximately 270,000 polyhedral elements, with a characteristic length of $\Delta = 0.30$ mm, located around the swirler exit plane, as defined in Eq.(3-22).
- Mesh 2: A fine mesh, consisting of approximately 2 million polyhedral elements, with a characteristic length of $\Delta = 0.13$ mm, located around the swirler exit plane.
- Mesh 3: A finer mesh, consisting of approximately 3.8 million polyhedral elements, with a characteristic length of $\Delta = 0.10$ mm, located around the swirler exit plane.

Note that these three meshes include a layer of elements around the surface, in order to describe the boundary layer flow. This layer has a characteristic thickness of $\Delta = 0.035$ mm.

Boundary conditions:

Two distinct boundary conditions at the swirler walls are also examined, in order to compare their impact on the swirl number and flow properties:

- BD1: No slip walls.
- BD2: Slip walls, i.e., zero shear stress condition at the walls.

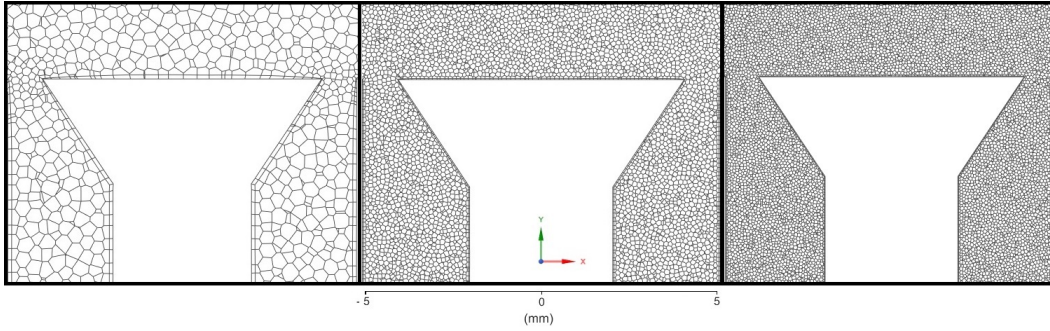


Figure 4.2: Detail of swirler exit section. From left to right: meshes 1, 2 and 3.

The purpose of this modification is to assess the need to describe the boundary layer flow in such a swirler configuration, also.

Turbulence modelling:

The influence of three turbulence models, commonly used in numerical studies of swirling flows, is also examined. Each of these models is presented and discussed in section 3.3.1.

- Realizable $k - \epsilon$.
- SST $k - \omega$.
- RNG $k - \epsilon$.

The isothermal studies in this section are performed using the whole computational domain, i.e., the swirler and combustion chamber. The meshing in the combustion chamber, away from the region close to the swirler exit surface, is considerably rough, since its properties are irrelevant to the present study. The fluid mixture properties are assumed constant: $\rho = 1.225 \text{ kg/m}^3$ and $\mu = 1.79 \cdot 10^{-5} \text{ kg/m.s}$ for density and dynamic viscosity, respectively. The total mass flow rate through the six combined inlet orifices is $\dot{m} = 0.001715 \text{ kg/s}$, which corresponds to a volumetric flow rate of $\dot{V} = 1400 \text{ cm}^3/\text{s}$, chosen to represent the higher values experimentally studied. Boundary conditions follow the procedure described in section 3.4.

Cases *a*, *b* and *c*, as summarized in Tab. 4.1, use the Realizable $k - \epsilon$ turbulence model, which has been chosen as the default for this work, and no slip boundary conditions at the swirler walls. The single difference between these three cases is the refinement of the computational grid, which progressively increases. Cases *b*, *d* and *e*, in a similar manner, differ from each other only in terms of the chosen turbulence models. The default meshing for these cases is mesh 2. Cases *b* and *f* directly compare the boundary conditions in the swirler walls, using the same mesh and turbulence model.

Upon examination of the results given in Tab. 4.1, it may be verified that the computed values of S range from 0.72 to 1.13. Reducing mesh spacing leads to smaller values of S and the discrepancy between meshes 2 and 3 is smaller than 5%. A 50% increase in the value of S has been obtained when slip boundary conditions are adopted at the swirler walls. The choice of a different turbulence model affects the computed value of S by less than 3%. Furthermore, the geometrical swirl estimate of $S = 0.4$, defined in Eq.(3-2), is significantly smaller than the calculated number obtained in all six cases. It may be inferred that the assumptions used in its formulation may over-simplify the flow properties distribution.

In order to allow for a more detailed comparison, the flow field within the swirler is now analysed. The swirling motion inside the swirler is represented in Fig. 4.3. The contours of the the z axis component of the flow velocity, which is the direction perpendicular to the evidenced section, indicate a counter-clockwise rotation inside this device. In the right side, contours in blue indicate a negative flow velocity in the z axis direction, whereas in the left side, contours in red indicate a positive flow orientation in z axis direction. A good symmetry between both sides may be perceived in all six cases. With the notable exception of case f , a small region close to the internal cylinder indicates the absence of swirling motion, most likely due to viscous forces and the downstream flow constraint at the bluff body vicinity.

Figure 4.3 also allows to verify that the solution of mesh 1, from case a , seems to result in an over-smoothing of the flow features due to higher turbulent viscosity in the swirling region, as indicated in Fig. 4.4, as compared to cases b and c . Qualitatively, very similar results from cases b and c may also be perceived, except for a slightly more symmetrical flow in the finer mesh case. This suggests, again, that mesh independency has been achieved for cases b and c . The three turbulence models results from cases b , d and e yield qualitatively similar results, which has also been evidenced in Tab. 4.1 by the similar values of the calculated swirl number. The slip walls boundary condition, in case f , led to the most particular outcome, as the absence of viscous dissipation at the walls results in higher velocity at the top region of the swirler, and, therefore, in a higher swirl number.

The over-smoothery of case a of the velocity field is also perceptible in the contours of the turbulent viscosity ratio from Fig. 4.4, which is the ratio between the turbulent viscosity μ_t and the molecular dynamic viscosity μ . The values of this property suggest that the flow turbulence is progressively reduced throughout the swirler. Indeed, the turbulent viscosity ratio is reduced from 70 to almost zero, which indicates a relaminarization of the bulk flow field and

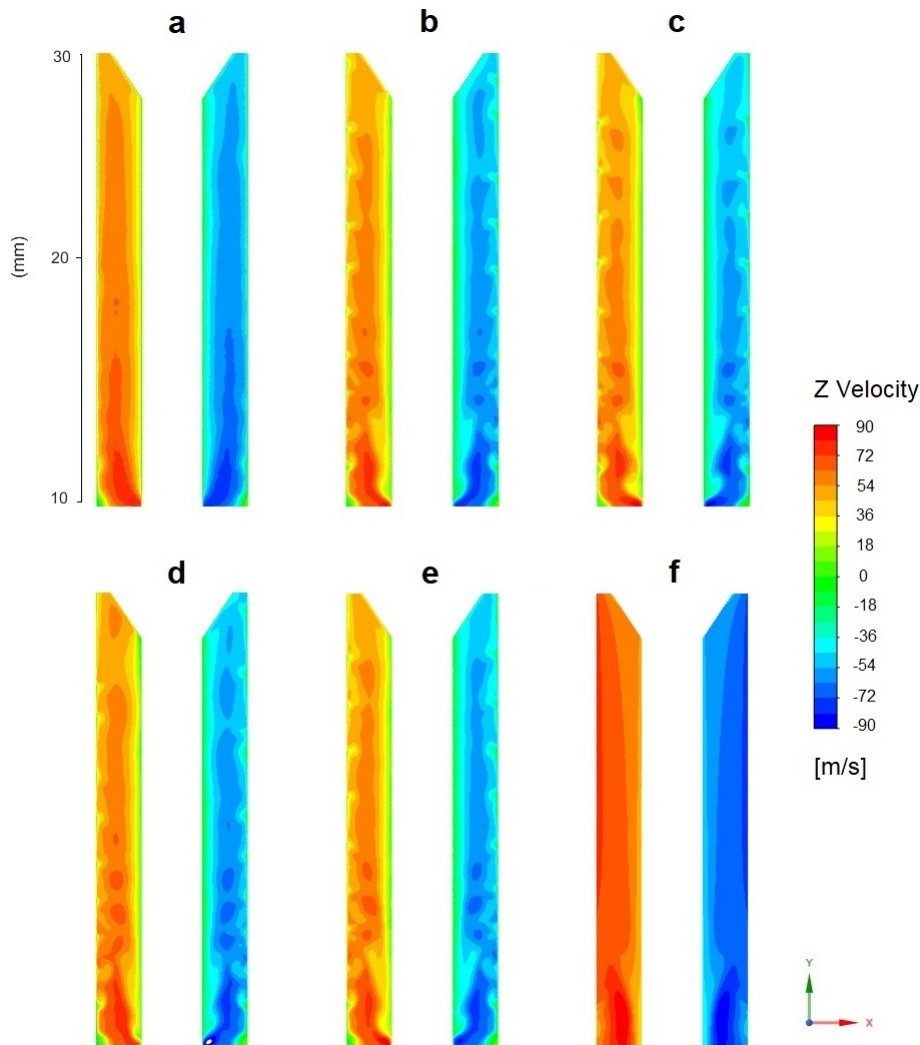


Figure 4.3: Contours of z velocity component at the planar section of the swirler, from inlet (bottom) to outlet (top) for 6 different cases, as described in Tab.4.1.

could explain the relative insensitiveness of the values of S on the choice of the turbulence model. This figure also allows to observe, in cases *b* and especially *c*, a trace of the swirling motion.

Further comparisons involving the vertical velocity component, in the direction of the y axis, may be seen in Fig. 4.5. Attention is drawn to the top part of the same swirler section as previously analysed, where a flow velocity increase occurs due to the presence of the bluff body. Two cases are directly compared: no-slip boundary condition (case *b*) and zero shear stress condition at the inner and outer walls of the swirler. The purpose of this comparison is to assess the need to describe the boundary layer flow in such a swirler configuration. A flow acceleration may be identified due to the flow narrowing upstream to the swirler exit.

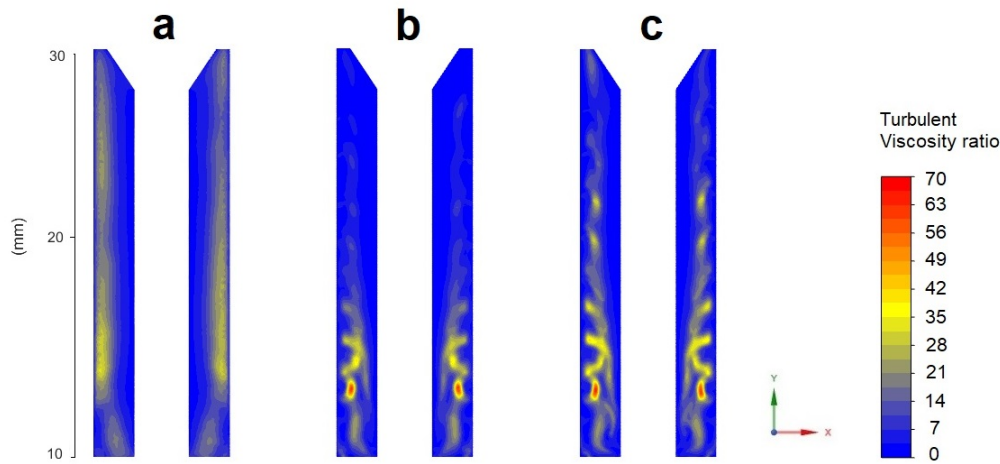


Figure 4.4: Contours of turbulent viscosity ratio in the planar section of the swirler, for 3 different meshing cases, *a*, *b* and *c*.

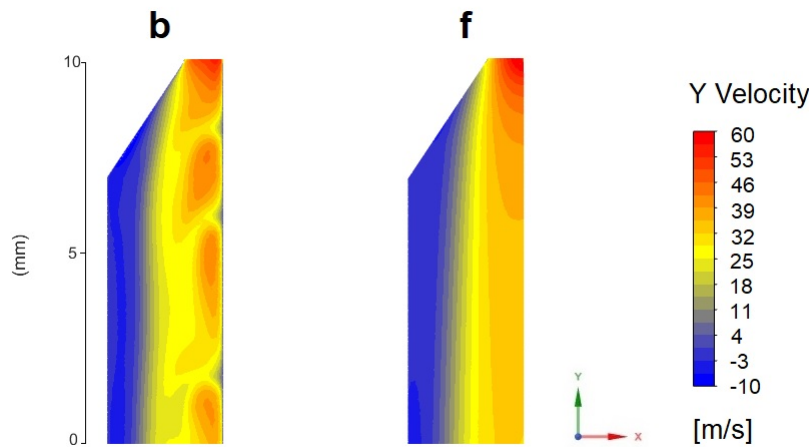


Figure 4.5: Contours of y velocity component at the planar section of the swirler, with detail on the top (exit) part. Two types of boundary conditions are compared: no slip walls (case *b*, left) and walls with zero shear stress (case *f*, right).

In both cases, a central recirculation zone (CRZ) may be perceived at the internal part of the annular section. The presence of this CRZ is unexpected and has not been addressed by the associated experimental works. Apparently, due to the occurrence of a vigorous swirling motion, the centrifugal effect dominates over other effects, and the centrifugal force drives the fluid outward to the sidewalls and creates an axisymmetric column-like “cavity” on the axis (55). Since the effects of viscous dissipation in walls are not present in case *f*, it may be inferred that the occurrence of such recirculation is not of a viscous nature, but of a pressure gradient related force. The rather large pressure

gradient in this same region may confirm this hypothesis, as illustrated in Fig. 4.6.

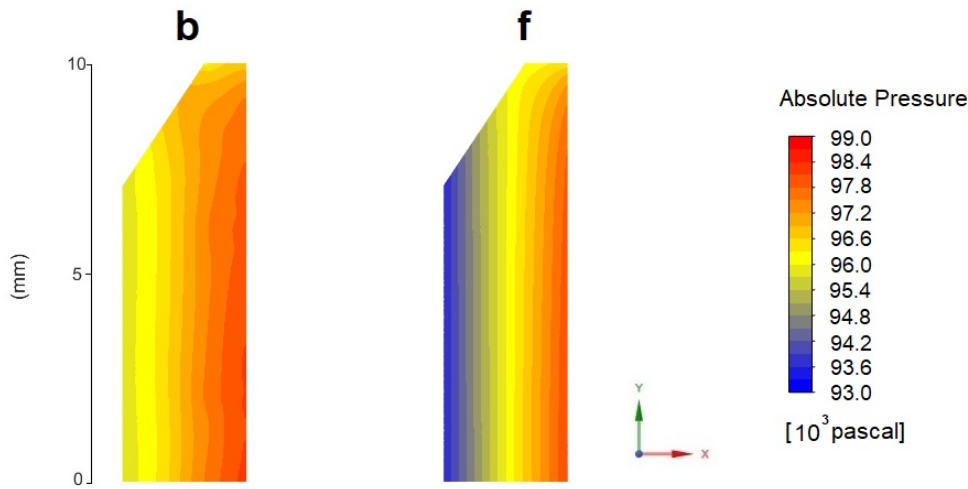


Figure 4.6: Contours of absolute pressure in the planar section of the swirler, with detail on the top (exit) part. Such as Fig. 4.5, cases of no slip walls (case *b*, left) and walls with zero shear stress (case *f*, right) are compared.

As an outcome of the present analysis, attention should be drawn to the swirler geometry, in particular to the bluff body cone angle, in order to avoid a CRZ. Such CRZ may indeed enhance the possibility of observing a flame flashback into the swirler, which could severely damage the combustion system (5).

An analysis of the flow structure at the swirler exit surface is now presented, for cases of no slip and zero shear stress walls. Contours of axial velocity, v_y , and tangential velocity, v_θ , are displayed in Fig. 4.7, at the swirler annular exit surface, for cases *b* and *f*, and the averaged circumferential values as a function of the surface radius is given in Fig. 4.8. As it may be seen, the velocity components distribution is non-uniform for all cases. Case *f* results are characterized by a circumferential symmetry, which is not observed for case *b*. Indeed, along the tangential direction v_y and v_θ exhibit, for case *b*, important non-uniformities which could be related to a reminiscence of the swirler orifices fluid passage. Investigating further this point has not been attempted. Note, also, that such non-uniformities could lead to unstable fluid motions, which are not captured by RANS simulations. Note, as it could be expected from mass conservation, that similar values of average axial velocity at the swirler exit ($\bar{v}_y \approx 49.5$ m/s) have been determined.

Further criticism on the assumptions used for determining the geometrical swirl number [Eq.(3-2)] may be exerted by examining the circumferentially

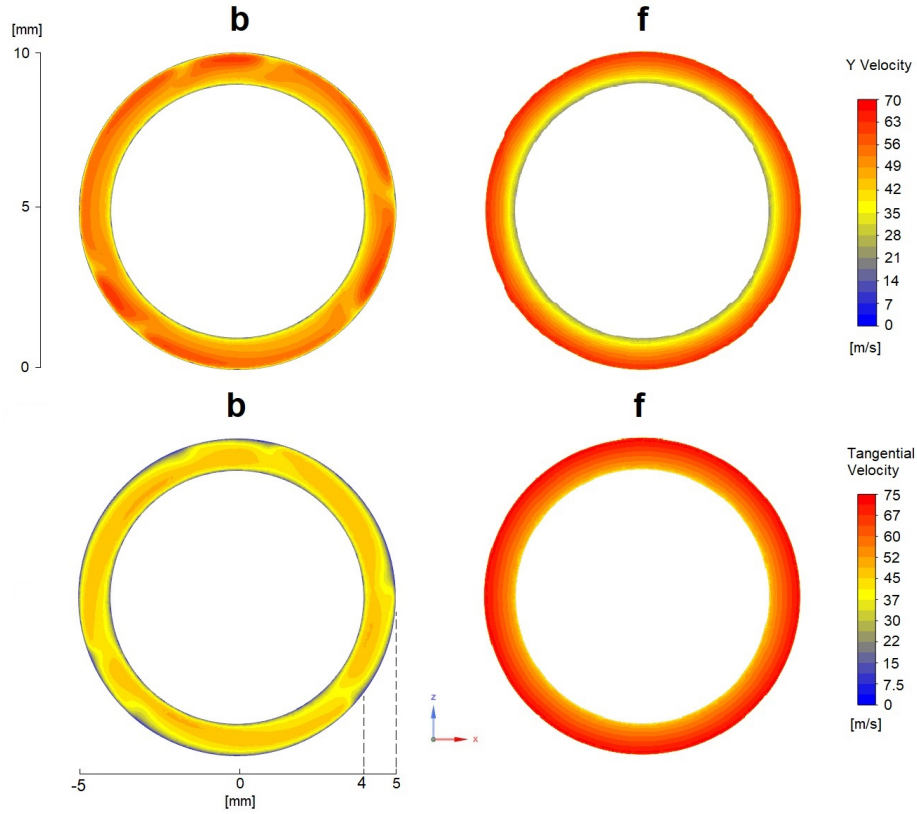


Figure 4.7: Contours of y velocity component (top) and tangential velocity component (bottom) for cases b and f , at the swirler exit surface, highlighted in Fig. 4.1.

averaged velocity components for cases b and f given in Fig. 4.8. Indeed, this figure allows to observe that, for the case of slip walls (f), the linear dependency of v_θ with r was a reasonable assumption, but the uniform v_y hypothesis used is clearly inadequate to describe the computed flow field. Concerning now case b , Fig. 4.8 results indicate that, within the bulk flow, v_y is a monotonically increasing function of r at the swirler exit, whereas v_θ exhibits a non monotonic behaviour. Both these functional dependencies seem to invalidate the simplifying assumptions used to derive the geometrical swirl number (13), of solid body rotation flow within the device, a uniform axial velocity and negligible pressure effects. Indeed, case b results suggest that more adequate behaviours could be given by $v_y \propto r$ and $v_\theta \sim \text{uniform}$.

The last flow analysis at the swirler region is the wall y^+ , represented in Fig. 4.9, for case b , at the external wall with the inlets and the internal wall with the bluff-body at its top. This non-dimensional distance is a parameter (16) commonly used for assessing the applicability of wall functions in turbulent models and is defined as:

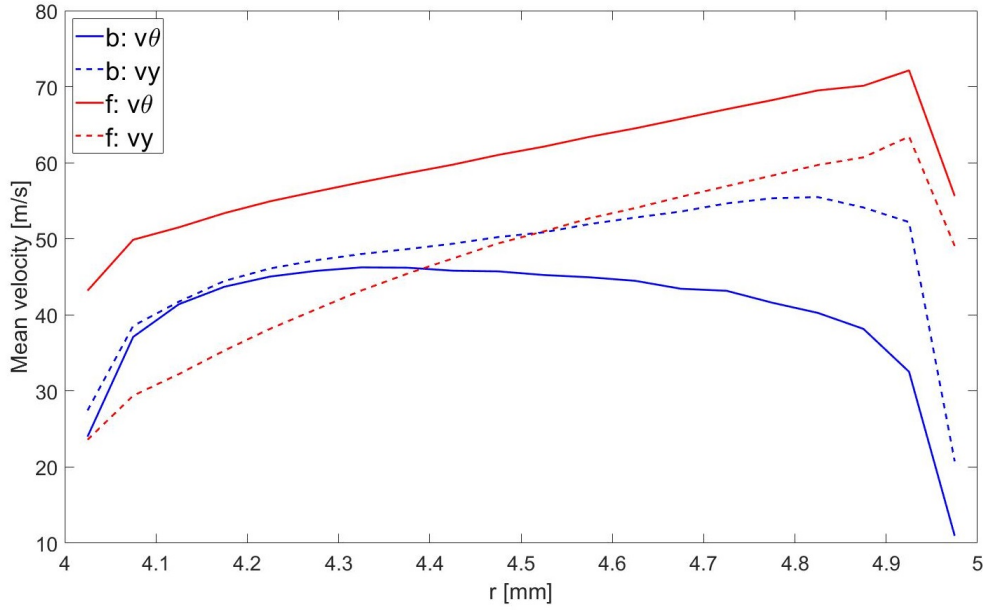


Figure 4.8: Circumferentially averaged values of y velocity component (dashed lines) and tangential velocity component (solid lines) at the exit surface, for cases b (blue) and f (red), as a function of the radius.

$$y^+ = \frac{yu_\tau}{\nu}, \quad (4-1)$$

where y is here (only) the distance normal to the wall, u_τ is the friction velocity and ν is the kinematic viscosity of the fluid. This non-dimensional length is directly proportional to the shear stress at the walls, which in turn is proportional to the fluid velocity adjacent to the wall. The higher shear stress at the external walls may also confirm the hypothesis that the centrifugal force drives the fluid outward in the swirler, creating the column-like cavity that causes the appearance of a CRZ. These streaks at the external wall, also perceptible in Fig. 4.5, indicate regions of stagnation which could be related to traces of the swirling motion reminiscent of the swirler orifices fluid passage, also.

As it may be noted, the y^+ distribution at the swirler walls ($0 < y^+ < 10$) indicates that a turbulence model wall function at the boundary layer may lead to incorrect predictions of the flow field at this region. Indeed, it has been pointed out that wall functions should be applied in the logarithmic boundary layer, i.e., when $y^+ > 30$ (56). Further investigations of this issue, as well as the relaminarization process depicted in Fig. 4.4, have not been attempted.

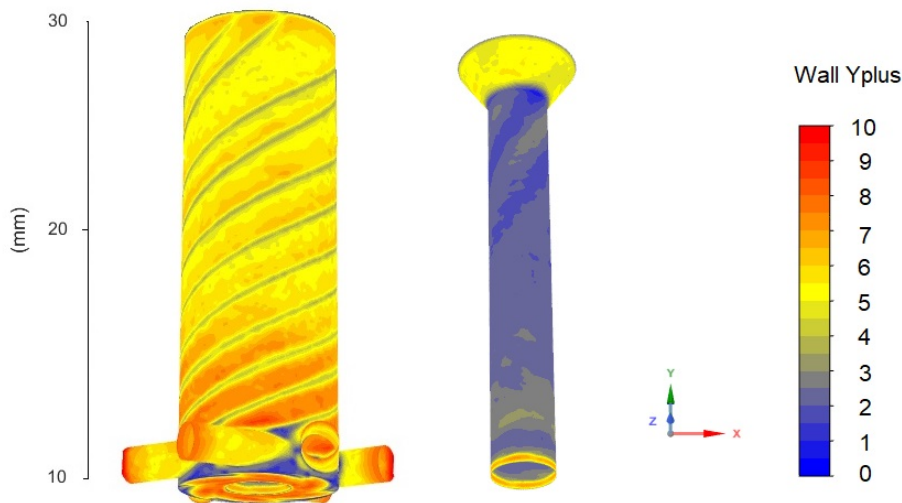


Figure 4.9: Contours of wall y^+ at the external walls with inlet orifices (left) and internal walls (right) of the swirler for case b .

4.2

Isothermal flow results

In order to understand the flow behaviour within the combustion chamber, non-reactive, isothermal, simulations are first performed. In the absence of chemical reactions and heat release, steady RANS simulations are expected to capture the average flow field structure. Although the precessing vortex core, an important flow structure found in swirling flows, exhibits a transient nature, and oscillatory mechanisms that cannot be captured by Reynolds-Averaged equations, steady RANS simulations in the literature have been shown to predict its average structure with reasonable accuracy (17). The flow field and turbulence properties within the combustion chamber are thus studied in this section.

Due to computational resources limitations, the meshing of the swirler region used in the following sections is a variation of mesh 1, described in the previous section, with a characteristic length of $\Delta = 0.30$ mm within the swirler region. A refinement is performed around the swirler exit plane, with a length of $\Delta = 0.10$ mm, as illustrated in Fig. 3.9. The meshing of the combustion chamber region has already been detailed in section 3.4. As it may be seen in Tab. 4.2, the swirl number obtained with this computational grid, using the Realizable $k - \epsilon$ turbulence model and no slip walls, is $S = 0.81$. All walls have no slip boundary conditions, and the fluid mixture properties and volumetric mass flow rate are the same as used in the previous section: $\rho = 1.225$ kg/m³

and $\mu = 1.79 \cdot 10^{-5}$ kg/m·s for density of fresh gases and dynamic viscosity, respectively.

Concerning the isothermal flow studies performed in this section, residuals have converged to a statistical steady state at significantly high values for the mass balance from the continuity equation, with an unscaled residual for the pressure-based solver of $R \approx 2 \cdot 10^{-1}$. The three velocity components have converged at a value of $R \approx 2 \cdot 10^{-4}$ m/s, for the Reynolds-Averaged Navier-Stokes equations. The k equation presented a residual value of $R \approx 8 \cdot 10^{-4}$, and the ϵ equation resulted in a residual of $R \approx 1 \cdot 10^{-3}$. These relatively high values of convergence residuals of the continuity equation could be influenced by several features, such as insufficient mesh sizing at the swirler and upper combustion chamber regions. The intrinsic transient nature of the precessing vortex core may also difficult the convergence process when steady RANS equations are applied. Further investigations to understand this occurrence have not been attempted.

As summarized in Tab. 4.2, the three choices of turbulence modelling, described in section 3.3.1, are compared, for the same meshing and boundary conditions, with respect to the flow field and turbulence properties within the combustion chamber. Note that these model choices are identical to those used for the swirler flow study in the preceding section.

Table 4.2: Isothermal studied cases of turbulence modelling influence.

Case	Turbulence model
a	Realizable $k - \epsilon$
b	RNG $k - \epsilon$
c	SST $k - \omega$

A three-dimensional representation of the recirculation zones present within the combustion chamber may be seen in Fig. 4.10. Using iso-surfaces of $v_y = 0$, it is possible to observe the region within which the flow is redirected towards the combustion chamber base. This figure also shows the streamlines, which allow to infer the fluid motion. The outer recirculation zones (ORZ) may be identified at the corners of the chamber, through recirculating streamlines inside the $v_y = 0$ surface at these corners. The inner recirculation zone (IRZ) may be seen around the computational domain center axis, and it is associated to a bubble-shaped surface of $v_y = 0$ and to the streamlines that outline this bubble and penetrate its top region. The main swirling jet may be seen between the ORZ and IRZ, at the lower part of the combustion chamber. This jet

expands downstream to the swirler exit, and interacts with the chamber walls. As it may be seen, the three choices of turbulence modelling yield qualitatively similar results.

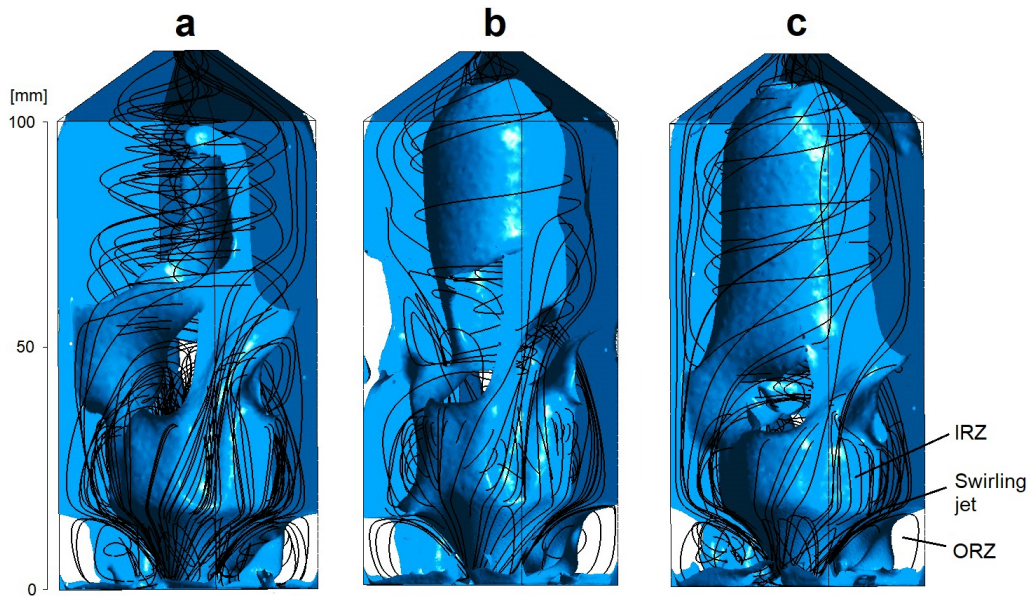


Figure 4.10: Representation of recirculation bubbles, through iso-surfaces of $v_y = 0$ m/s (blue), with superimposed streamlines from the swirler exit (black), for isothermal cases *a*, *b* and *c*, summarized in Tab. 4.2.

It is also possible to identify recirculation bubbles at the combustion chamber upper region in Fig. 4.10, especially in cases *b* and *c*. At a height of $y = 100$ mm, a region of fluid redirected towards the base may be noted for these cases, which underscores the influence of the convergent pyramid-shaped structure at the top of the combustion chamber. Indeed, the cross sectional narrowing upstream to the domain exit effectively closes the recirculation bubble due to the flow acceleration. The results obtained when this feature is absent led to reverse flow at the domain exit, which hinders the converging process. Note that non-reactive experimental results are not available for comparison purposes.

The flow field within the combustion chamber in the absence of chemical reaction is now analyzed in Fig. 4.11, in terms of the vertical velocity component (v_y) contours. This planar section is the same as depicted in Fig. 4.2. The ORZ and IRZ may be observed as regions of negative values of the vertical velocity component. Confirming the discussion developed in the light of Fig. 4.10, it is possible to observe the swirling jet expansion upon exiting the swirler, in the region between the ORZ and IRZ. This jet impacts the combustor walls and is deflected upwards and downwards. In all three cases, it is

possible to observe a flow of high velocity magnitude ($v_y \approx 20$ m/s) adjacent to the combustion chamber walls. Such high velocity values should be associated to high convective heat transfer rates in the presence of combustion. The three turbulence models yield qualitatively similar results. Notice, however, that the realizable $k - \epsilon$ model, case a , presents the most symmetrical flow field.

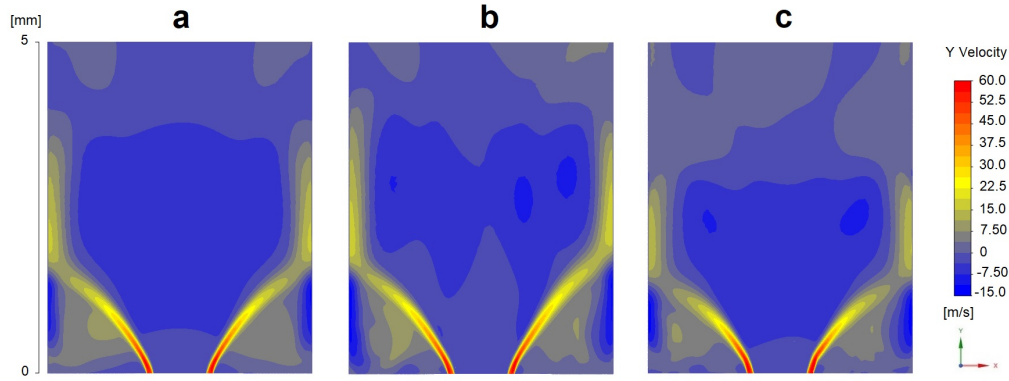


Figure 4.11: Contours of y velocity component at the planar section of the lower combustion chamber region for cases a , b and c , summarized in Tab. 4.2.

Further analysis of the flow field and turbulence properties at the lower part of the combustion chamber, downstream to the swirler exit, is possible by examining the results given in Fig. 4.12, for the three studied turbulence models summarized in Tab. 4.2. The top three contours depict the velocity field in the horizontal direction, i.e., v_x . The expansion of the swirling jet away from the swirler exit to the chamber walls may again be observed, through a high velocity magnitude in the horizontal direction ($v_x \approx 30$ m/s). The three turbulence models yield qualitatively similar results, though a small variation in the height of the expanding jet is noticeable. Indeed, Fig. 4.11 allows to observe that the heights where the swirling jet contacts the chamber walls are $y = 15$ mm, $y = 15$ mm and $y = 13$ mm for cases a , b and c , respectively. The turbulent viscosity ratio, with a color scale emphasis at the ORZ and swirling jet regions, is also compared in this figure for the three cases. This property ratio is similar to a turbulent Reynolds number, which is a parameter that directly controls the turbulent combustion regime, as discussed in chapter 3. The values of this property suggest that the flow turbulence in the ORZ is $\mu_t/\mu \approx 30$ for case a and $\mu_t/\mu \approx 20$ for cases b and c . It may be expected for the flow thermal expansion due to combustion to decrease those values. The last comparison in Fig. 4.12 is the transported turbulent kinetic energy k , which describes the energy of the turbulent fluid motion. It may be noted that the turbulent kinetic energy is concentrated at the swirling, expanding

jet for all three cases. The $k - \omega$ turbulence model, from case c , presents a higher value of k at this location than the other models, with a peak value of $k \approx 180 \text{ m}^2/\text{s}^2$.

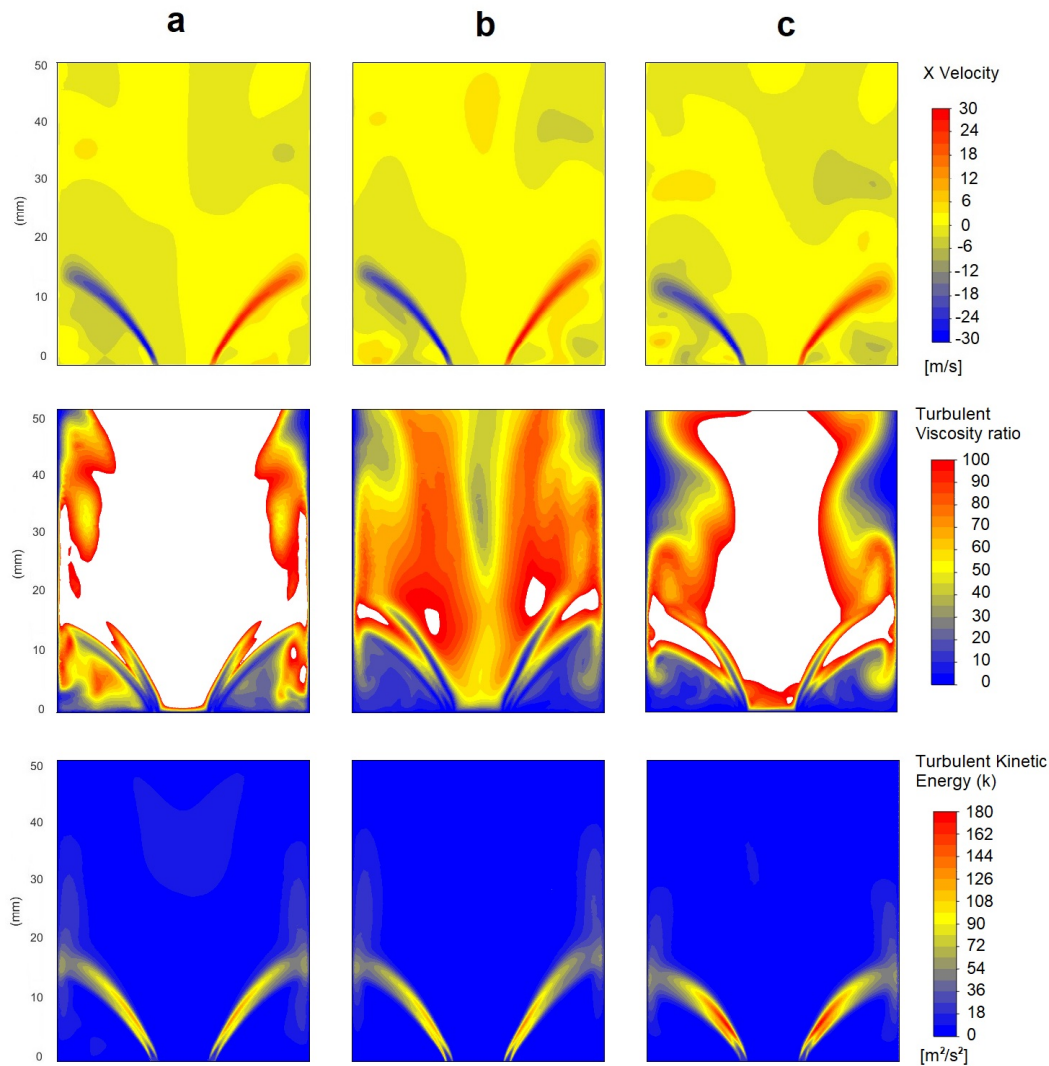


Figure 4.12: Contours of x velocity component (top), turbulent viscosity ratio (middle) and turbulent kinetic energy (bottom), at the planar section of the lower combustion chamber region for cases a , b and c , summarized in Tab. 4.2.

4.3

Reactive flow results

The reactive flow results described in this section have been carried out with the realizable $k - \epsilon$ turbulence model. As seen in the preceding sections, the three turbulence models have yielded similar qualitative results, in terms of the flow field and turbulence properties. Since qualitatively similar results have been obtained for the isothermal flow simulations and no experimental

data is available for these flow properties, it is impossible to determine the most adequate turbulence model for this studied system by examining the obtained results only. The realizable $k - \epsilon$ is, then, chosen, as it has been pointed out in the literature as the most predictive two-equation model for high swirling flows, with the best agreement with experimental results (19). The premixed combustion Extended Coherent Flamelet Model is applied in all results, except when otherwise stated, for comparison purposes with the Zimont turbulent flame closure model, both of which have been described in chapter 3. The unburnt fluid mixture properties, such as in the isothermal studies of the previous sections, are $\rho = 1.225 \text{ kg/m}^3$ and $\mu = 1.79 \cdot 10^{-5} \text{ kg/m}\cdot\text{s}$ for density of fresh gases and dynamic viscosity, respectively. The temperature of the unburnt gases is $T_u = 300 \text{ K}$. The same total mass flow rate from the isothermal studies is used, also: $\dot{m} = 0.001715 \text{ kg/s}$, which corresponds to a volumetric flow rate of $\dot{V} = 1400 \text{ cm}^3/\text{s}$. Boundary conditions follow the procedure described in the preceding section. The pressure-based coupled algorithm is again used for pressure-velocity coupling.

Two flame topologies are numerically defined and characterized in this section: flame regimes IV (outer recirculation zone flame) and II (unstable flame) [(12), (13) and (14)]. The equivalence ratio values of the numerically obtained flame topologies do not directly correspond to their experimental counterparts. Indeed, the values of ϕ for the numerical results are $\phi = 0.83$ and $\phi = 0.70$ for regimes IV and II, respectively, whereas the corresponding experimental values are $\phi = 0.73$ and $\phi = 0.62$. Further decreasing of the equivalence ratio below $\phi = 0.70$ has led to numerical instability, and a consequential flame blow-off. This is possibly due to insufficient mesh sizing at the upper part of the combustion chamber, since leaner flames tend to be longer and detach from the combustion chamber base. The shorter combustion chamber used in this study ($H_c = 100 \text{ mm}$), with respect to its experimental counterpart ($H_c = 170 \text{ mm}$), may also hinder the numerical convergence of this longer flame.

4.3.1

Flame regime IV: Outer Recirculation Zone flame (M-flame)

The results presented in this section concern the flame topology IV. The flow field within the combustion chamber is first analysed. Fields of turbulence and combustion-related properties are then discussed and compared with the isothermal results presented in section 4.2. Comparisons with experimental results are then performed, in terms of the average flame location.

4.3.1.1

Overall flow structure

The flame regime treated in this section is known as Flame IV, briefly described in section 2.1, and defined and characterized experimentally in the literature [(12), (13) and (14)]. At the highest equivalence ratio experimentally studied, the average flame brush is located around the swirling, expanding jet and at the outer recirculation zones, i.e., at the vicinity of four corners of the combustion chamber. In order to numerically obtain this flame topology, a methane/air equivalence ratio of $\phi = 0.83$ is used, for which the values of adiabatic combustion temperature and laminar flame velocity are $T_b = 2000$ K and $U_l = 30.0$ cm/s, respectively. Since at this equivalence ratio the flame exhibited stability during the converging process, the steady RANS approach has been adopted.

A three-dimensional representation of the recirculation bubbles may be seen in Fig. 4.13. The upper recirculation bubble, which may also be observed in the isothermal flow studies, in Fig. 4.10, is closed, due to the flow acceleration associated to the chemical reaction heat release. As it may be seen, the swirling jet quickly expands after the swirler exit, between the IRZ and ORZ, and interacts with the chamber walls. The contours of the vertical velocity component, v_y , show that the swirling jet detaches from the chamber walls, after overcoming the IRZ, as an influence of the recirculating fluid, at a height of $y \approx 50$ mm. This behaviour affects the resulting average flame location within the combustion chamber, especially in cases of leaner mixtures, as it will be seen in the forthcoming sections.

The flow field within the combustion chamber is now studied. The swirling jet expansion and recirculation are represented in Fig. 4.14, through contours of the vertical velocity component, v_y , at planes located at heights $y = 0, 10, 20, 30$ and 40 mm, from the combustion chamber base. A good 45° symmetry may be observed, i.e., with respect to the four corners of the combustion chamber. As it may be confirmed from the regions of high velocity in the positive direction of the y axis, the jet expands from the swirler exit and interacts with the chamber walls, at a height between $y = 10$ mm and $y = 20$ mm. An outer recirculation zone (ORZ) can be seen at the four corners of the chamber beneath this height, represented by a flow redirection towards the base. Both the expansion and swirling motion also generate a pressure deficit at the center of the computational domain, not shown here for the sake of brevity, which causes an inner recirculation zone (IRZ), represented by a flow redirection towards the swirler buff-body also.

Further analysis of the flow field, turbulence and combustion properties

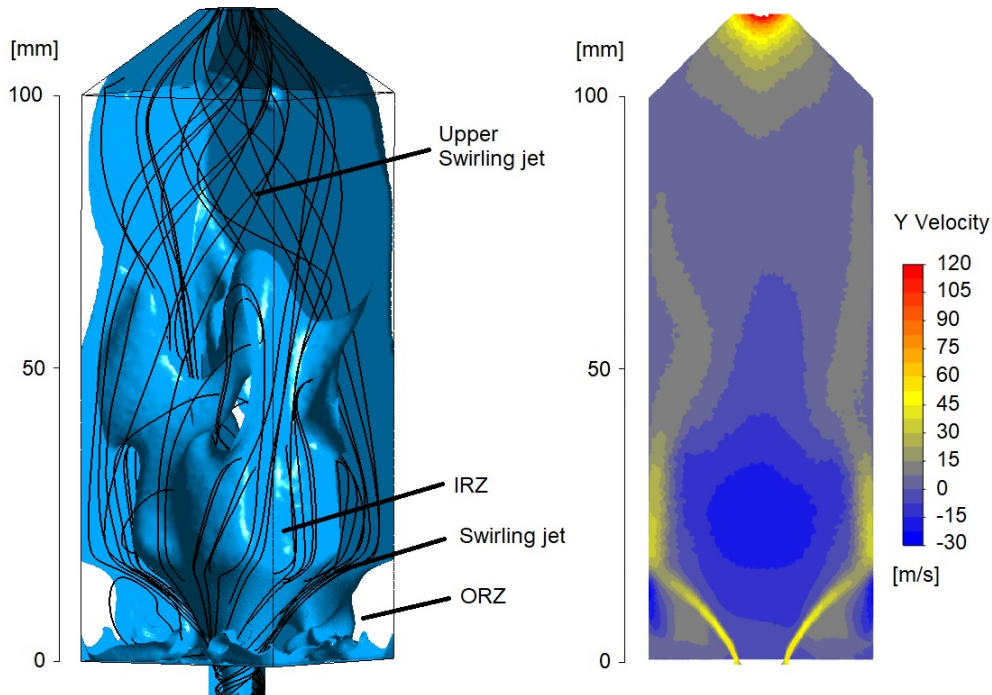


Figure 4.13: Representation of recirculation bubbles, through iso-surfaces of $v_y = 0$ m/s (blue), with superimposed streamlines from the swirler exit (black) (left) and contours of vertical velocity component, v_y , at the combustion chamber section (right).

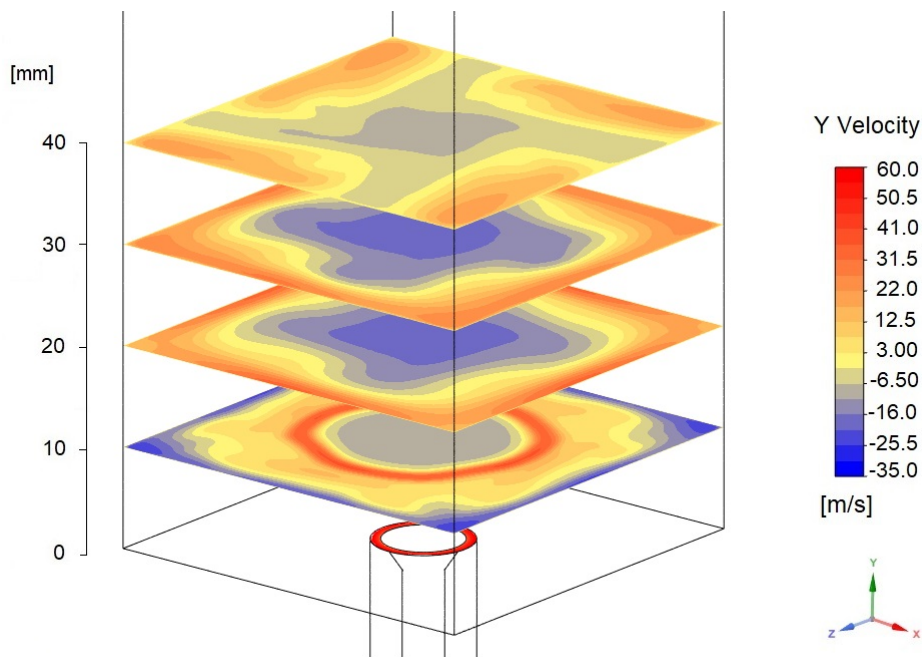


Figure 4.14: Contours of vertical velocity for heights $y = 0, 10, 20, 30$ and 40 mm, from the combustion chamber base.

at the lower part of the combustion chamber, downstream to the swirler exit, is possible by considering the results illustrated in Fig. 4.15. Figure 4.15(a) and (b) depict the velocity field in the vertical and horizontal directions, i.e., v_y and v_x . It may be observed, in greater detail than in Fig. 4.14, the expansion of the swirling jet from the swirler exit to the chamber walls. The inner and outer recirculation zones may be perceived also, from the flow redirection towards the combustor base. Fig. 4.15(c) gives the temperature field at the outer recirculation zone. As it may be seen, a recirculation of hot gases, at $T \approx 1300K$, occurs in this region, which is the main characteristic of this flame regime (14). From Figs. 4.15(a) and (c), a flow of high velocity magnitude of hot gases adjacent to the chamber walls may be identified also. It could be inferred that the used assumption of zero heat flux at the walls in the boundary conditions may lead to an under-prediction of the heat flux near the walls and, therefore, to an incorrect temperature distribution. Figure 4.15(d) depicts the turbulent viscosity ratio, with an emphasis at the ORZ and swirling jet regions. The values of this property suggest that the flow turbulence in the ORZ is $\mu_t/\mu \approx 10$, which represents a modest turbulence level. From Fig. 4.15(e), it may be seen that the values of Da are significantly low ($Da < 1$) in the swirling jet upstream to the flame. This indicates that, according to this Da estimation, this flame could be situated in the thickened flamelet regime in the Borghi diagram from Fig. 3.5, which would not be suited for the coherent flame model applied here. Note that this Da estimate is based on an order of magnitude analysis of the thermal flame thickness from Eq.(3-7), which could differ from the value computed using detailed chemistry and transport by an order of magnitude (57). These issues are currently under scrutiny and will be fully addressed in future works. Figure 4.15(f) depicts the distribution of the flame surface density, Σ , computed by solving Eq.(3-16), which indicates that the flame surface lies around the fuel/air swirling jet and, again, exhibits a strong interaction with the wall.

Further analysis of the properties illustrated in Fig. 4.15 is possible by comparison with the isothermal flow results, depicted in Figs. 4.11 and 4.12. An analysis of the corresponding vertical velocity fields indicate similar values of v_y downstream to the swirler exit, which is expected due to flow continuity. The velocity magnitude of the jet adjacent to the walls, in the positive and negative directions (ORZ), is significantly higher in the reactive case. This has also been expected, as the thermal expansion of the combustion process accelerates the fluid mixture. In the reactive case, the IRZ extension is smaller, due to the increased intensity of the swirling jet around it. The corresponding velocity magnitude is, therefore, significantly higher. The turbulent viscosity

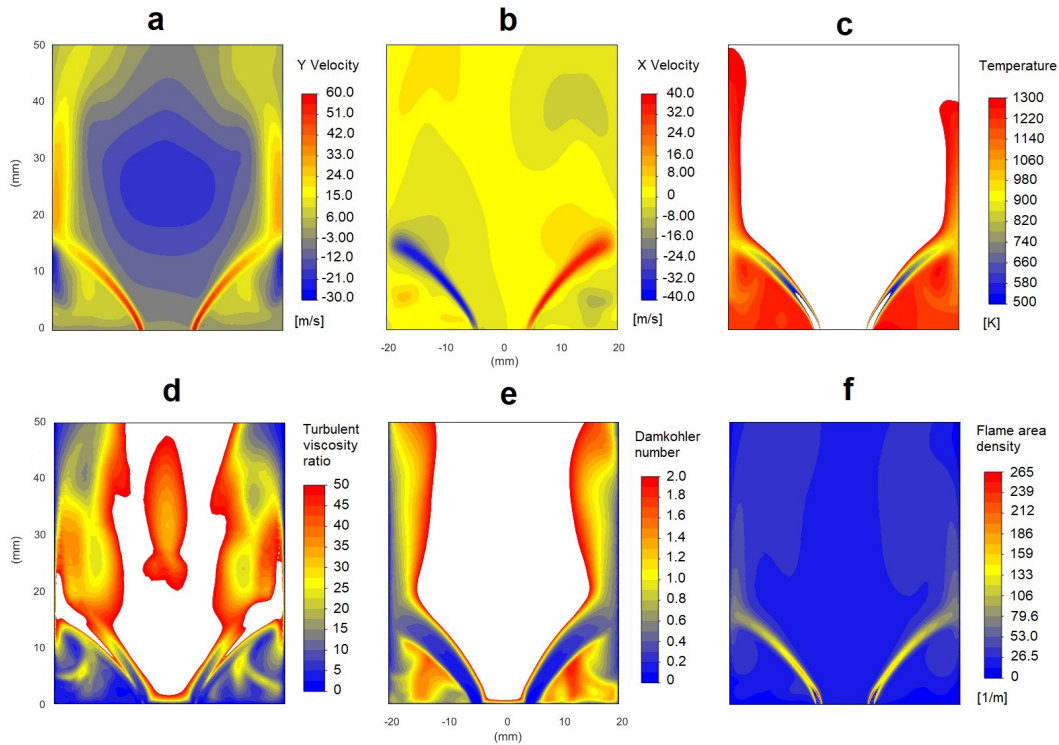


Figure 4.15: Contours of flow and combustion properties. (a): vertical velocity; (b): horizontal velocity; (c): temperature field at the ORZ; (d): turbulent viscosity ratio at the swirling jet and ORZ; (e): Damköhler number at the swirling jet and ORZ; (f): flame surface density (Σ).

ratio in the reactive case is also noticeably smaller than in the isothermal flow counterpart. Indeed, this is associated to the value of the dynamic viscosity, μ , which increases with the fluid mixture temperature. The value of μ_t/μ , therefore, decreases in the presence of heat release from the combustion process.

0

4.3.1.2 Comparison with experimental results

In order to gain further insight of the flame topology, a comparison between numerical and experimental results for a representation of the average flame brush is given in Fig. 4.16. The experimental instantaneous PLIF-OH signal has been binarized, assuming a zero value when OH is absent, and one when OH is present (12). As a consequence, the binarized results should represent a progress variable, where $c = 0$ denotes fresh gases and $c = 1$ denotes burnt gases, obtained from Eq.(3-11). The average value of this property should then represent the mean flame surface. For this studied flame, the topology is that of an outer recirculation zone flame (14), where the flame surface stabilizes

around the expanding jet, ORZ and chamber walls. The equivalence ratio used to obtain this experimental result is $\phi = 0.73$, i.e., smaller than that used in the present computations ($\phi = 0.83$).

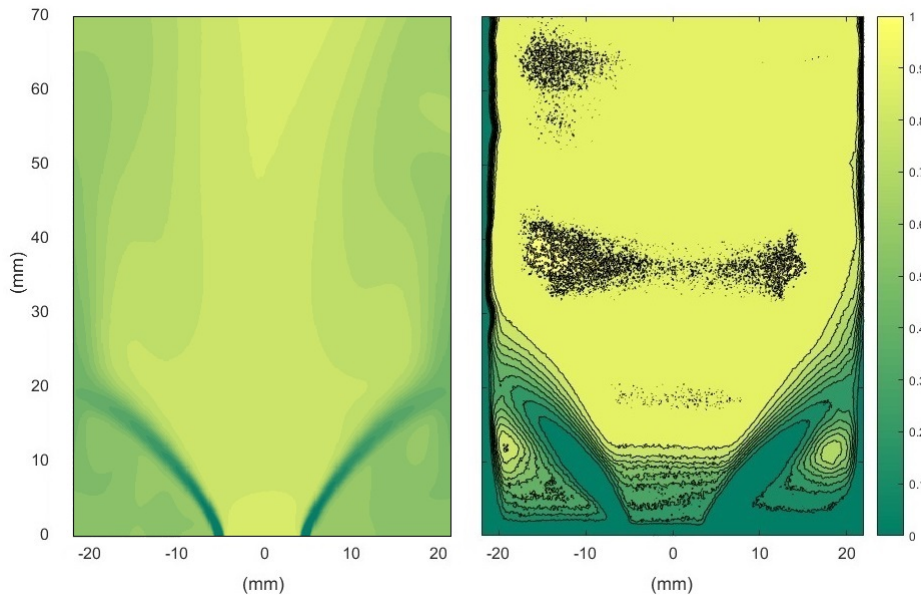


Figure 4.16: Flame regime IV: contours of computed progress variable (left) and average OH radical binarized image, measured with PLIF (right), adapted from (13).

As it can be seen from Fig. 4.16, the computed progress variable field predicts the average flame around the expanding jet and outer recirculation zones. In the ORZ, the mean progress variable value is $c \approx 0.5$, and downstream to the swirling jet $c \approx 0.8$. The flame expands and starts to interact with the combustion chamber walls at similar positions, $y \approx 15$ mm, from the chamber base. The agreement between the model and the experiments is qualitative. In particular, the average flame brush thickness obtained experimentally ($\delta \approx 3$ mm) may be seen to be larger than the computed counterpart ($\delta \approx 1$ mm). This quantity is estimated from the transitional space between fresh gases and burnt gases, normal to the flame front. Nevertheless, the overall position of this flame front is adequately predicted. The obtained discrepancies could be due to the above mentioned model shortcomings.

The progress variable field has also been computed with the Zimont Turbulent Flame Closure Model, using the same configuration that for the Extended Coherent Flamelet Model from Fig. 4.16. A comparison with the same flame topology IV obtained experimentally may be seen in Fig. 4.17. As it may clearly be observed, the one-equation model largely under-predicts the flame surface area within the combustion chamber, thus underscoring this

model inadequacy to predict the available experimental data. Therefore, this model will not be used in the following sections.

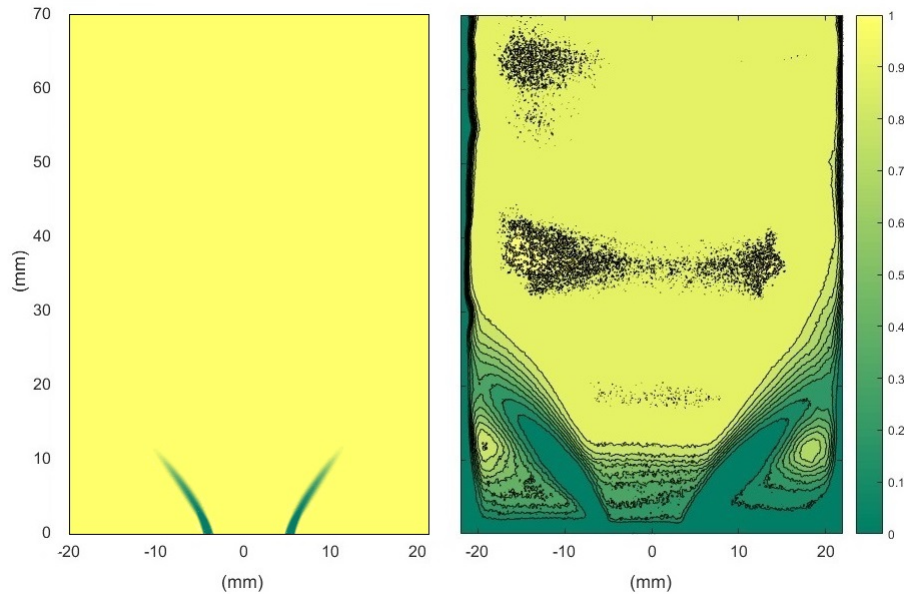


Figure 4.17: Flame regime IV: contours of computed progress variable using the Zimont Turbulent Flame Closure model (left) and average OH radical binarized image, measured with PLIF (right), adapted from (13).

4.3.2

Flame regime II: Instability region

The results presented in this section concern the flame topology II. The flow field within the combustion chamber is first analysed. Fields of turbulence and combustion-related properties are then discussed and compared with the isothermal results presented in section 4.2. Comparisons with experimental results are then performed, in terms of the average flame properties.

4.3.2.1

Overall flow structure

The flame regime treated in this section is known as Flame II [(12), (13) and (14)]. As the equivalence ratio decreases, this flame regime occurs in the transition between stable regimes III (V-Flame) and I (Tornado Flame). The flame brush location is unstable, as it pulses between the upper swirling jet and the inner recirculation zone, resembling the flame regimes I and III intermittently. In order to numerically obtain this flame topology, a methane/air equivalence ratio of $\phi = 0.70$ is used, for which the values of adiabatic combustion temperature and laminar flame velocity are $T_b =$

1840 K and $U_l = 20.0$ cm/s, respectively. Again, the two-equation Extended Coherent Flamelet Model has been applied to describe this regime. Due to the expected unsteady behaviour, transient (unsteady) RANS has been employed. Notice that RANS equations are not expected to fully predict the turbulent combustion instability nature, but could yield an overall indication of the instability onset. Most of the recent studies of thermoacoustic instabilities do indeed employ Large Eddy Simulations, as discussed in chapter 2.

The instantaneous recirculation bubbles representative of this flame regime may be seen in Fig. 4.18. Such as in regime IV, the upper recirculation bubble is closed, due to the flow acceleration associated to the heat release of thermal expansion. The swirling jet detaches from the chamber walls also, after passing through the IRZ, as an influence of the recirculating fluid. Since the laminar flame speed is smaller than in the previous case, due to a leaner premixed mixture, a smaller amount of burnt gases is expected to be observed at this high velocity region, i.e., at a height of $y \approx 50$ mm around the chamber walls, with respect to the recirculation zone.

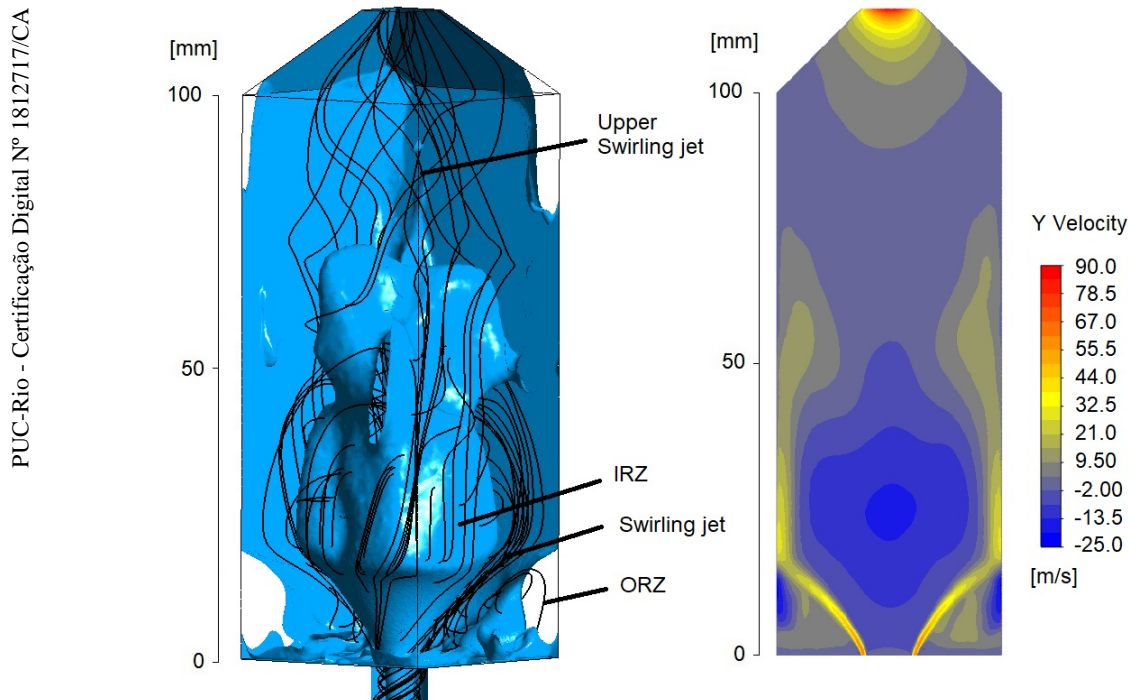


Figure 4.18: Representation of recirculation bubbles, through iso-surfaces of $v_y = 0$ m/s (blue), with superimposed streamlines from the swirler exit (black) (left) and contours of vertical velocity component, v_y , at the combustion chamber section (right).

The swirling jet expansion and recirculation is represented in Fig. 4.19 for the flame regime II. Contours of the vertical velocity component, v_y ,

are exhibited at heights $y = 0, 10, 20, 30$ and 40 mm, from the combustion chamber base, taken at a particular, arbitrary, instant. Such as in Fig. 4.14, an outer recirculation zone (ORZ) can be seen at the four corners of the chamber, and an inner recirculation zone (IRZ) around the domain center axis. Due to the transient behaviour characteristic of this swirling flame regime, a 45° symmetry is not observed, i.e., with respect to the four corners of the combustion chamber. The velocity of the expanding jet and the recirculating fluid are smaller in magnitude, with respect to those observed at the regime IV, from Fig. 4.14. This could be due to the smaller amount of heat released by the leaner premixed flame.

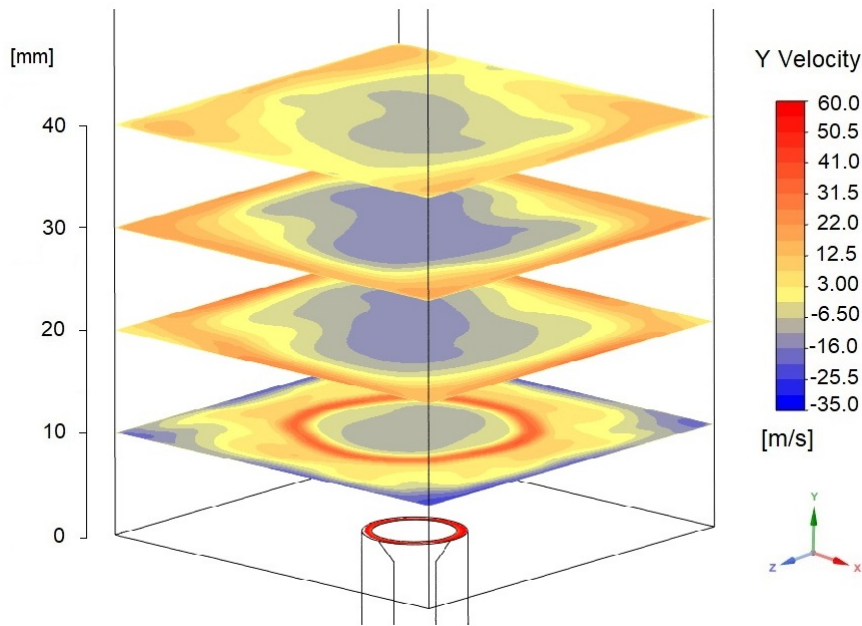


Figure 4.19: Contours of vertical velocity for heights $y = 0, 10, 20, 30$ and 40 mm, from the combustion chamber base.

The flow field, turbulence and combustion properties are illustrated in Fig. 4.20 for the flame regime II also, at the lower part of the combustion chamber. The velocity field in the vertical direction, v_y , depicted in Figure 4.20(a), indicates significantly lower velocity magnitudes at the expanding jet and the recirculating zones, with respect to the flame regime IV results given by Fig. 4.15. The mean temperature at the ORZ and the flame area density contours [Figs. 4.20(c) and (f), respectively] also exhibit lower values ($T \approx 800$ K), with respect to flame with a higher equivalence ratio. The smaller value of U_l for the leaner combustion leads to a smaller value of Σ from Eq.(3-16), which then leads to a smaller prediction of the flame surface density and propagation. The horizontal velocity field, i.e., v_x and Damköhler number fields, from

Figs. 4.20(b) and (e), respectively, yield qualitatively similar results, with respect to flame regime IV.

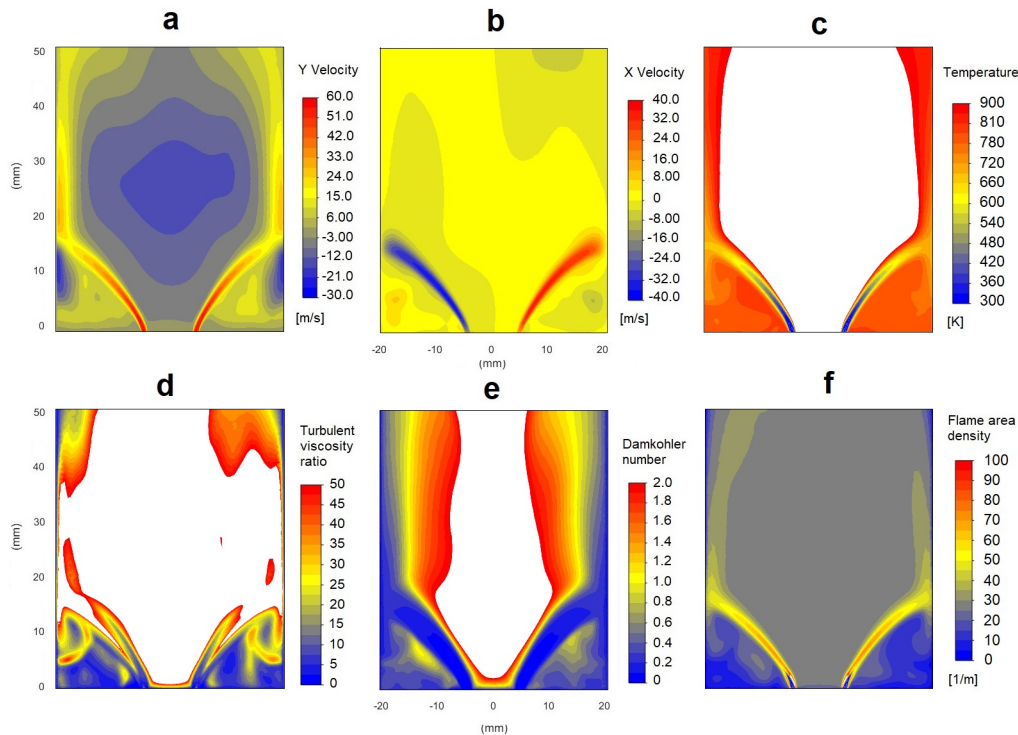


Figure 4.20: Contours of flow and combustion properties. (a): vertical velocity; (b): horizontal velocity; (c): temperature field at the ORZ; (d): turbulent viscosity ratio at the swirling jet and ORZ; (e): Damköhler number at the swirling jet and ORZ; (f): flame surface density (Σ).

4.3.2.2

Comparison with experimental results

The obtained flame topology is compared with the experimental results in Fig. 4.21. A total of 200 instantaneous images from the transient RANS solver, within a time range of $\Delta t = 60$ ms have been averaged, in order to obtain a representation of the flame brush location. The average flame is found to oscillate between the inner recirculation zone and the upper swirling jet, intermittently detaching from the combustion chamber base. These results are not given here for the sake of brevity. As a consequence of this behaviour, two local maximum values of the progress variable may be observed at the domain center: at the IRZ ($c \approx 0.6$), between the expanding jets and at the upper swirling jet, near the domain exit. Experimentally, the peak value of the binarized, averaged OH fluorescence is $c \approx 0.8$. A small amount of burnt gases is perceived at the ORZ at the computed progress variable ($c \approx 0.2$), whereas no OH is experimentally registered at the ORZ. A smaller value of c

is noticeable at regions of positive v_y , at a height of $y \approx 50$ mm, as it has been evidenced in Fig. 4.18, in both numerical and experimental results. Such as in the flame regime IV, the average flame brush thickness obtained experimentally ($\delta \approx 3$ mm) seems to be larger than the computed counterpart ($\delta \approx 2$ mm). Nevertheless, the qualitative agreement of modeled and experimental results is remarkable.

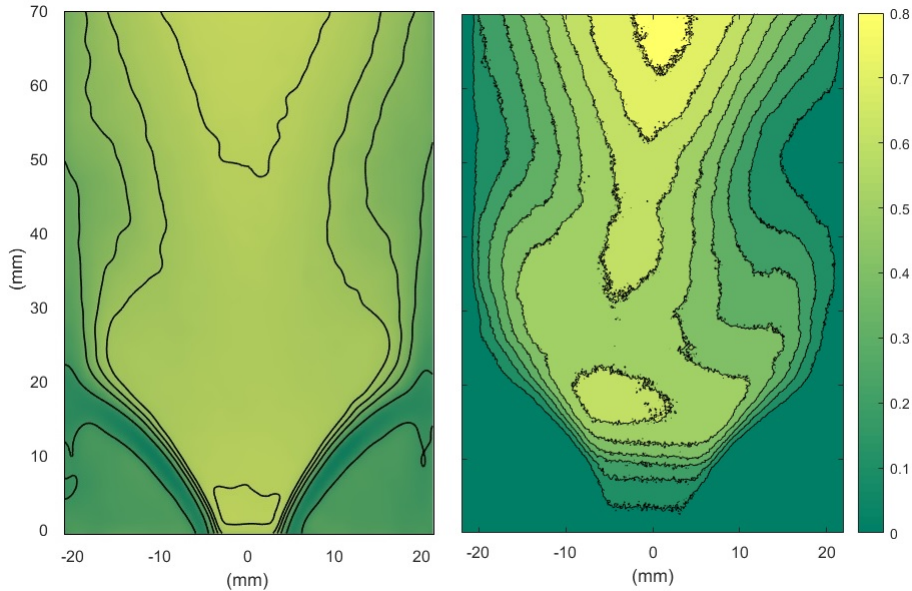


Figure 4.21: Flame regime II: contours of computed progress variable (left) and average OH radical binarized image, measured with PLIF (right), adapted from (13).

4.4 Borghi diagram analysis

An analysis of flames IV and II behaviour, with respect to the flame/turbulence interaction, is given in Fig. 4.22. The ellipses locations, which delimit the flame regimes have been estimated from the turbulent Reynolds number, obtained from Eq. (3-8), and the ratio between the root-mean-square and the laminar flame speed, u'/U_l , obtained from Eq. (3-5). These results indicate that these flames could be situated in the thickened flamelet regime within the Borghi diagram, which has been discussed in section. 3.3.2. This classical turbulence/combustion interaction regime is expected to occur for Damköhler number values smaller than one and, thus, correspond to an instantaneous flame structure significantly departs from the laminar flamelet one. Therefore it could be inferred that the studied turbulent premixed flame would not be suited for predictions using the coherent flame model applied

here. As discussed in section 4.3.1, this turbulent Reynolds number estimate is based on an order of magnitude analysis of the thermal flame thickness from Eq. 3-7, which could differ significantly from the value computed using detailed chemistry and transport. However, determining the suitability of the ECFM for predicting the studied flames would require the availability of more detailed experimental data, such as velocity measurements.

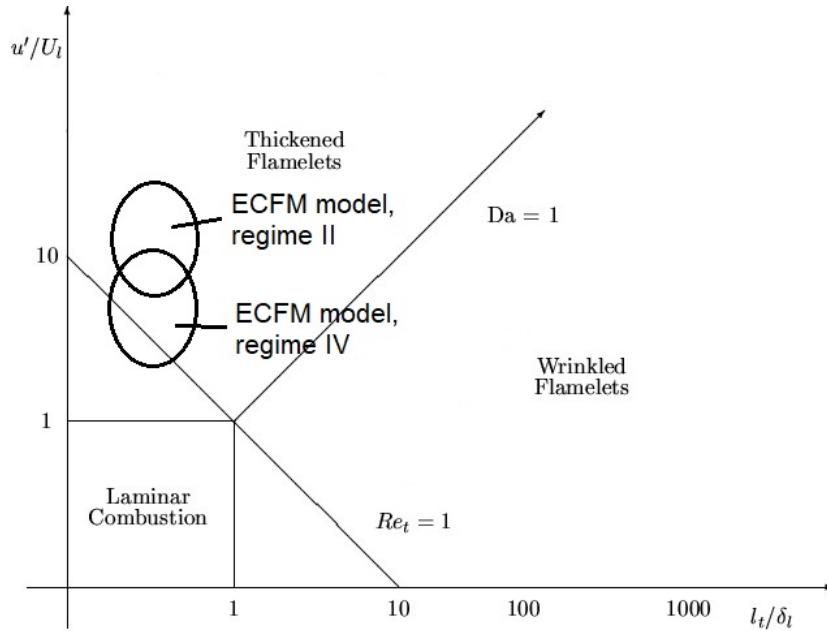


Figure 4.22: Simplified Borghi diagram for turbulent premixed combustion. Adapted from (43). The computed flame regimes locations at the diagram are given by the ellipses.

5 Conclusion and Perspectives

The numerical study of turbulent, premixed flames within a radial swirler and a square-sectioned combustion chamber has been performed in this work. This study aimed to model, using the RANS approach, the lean premixed turbulent swirling combustor developed at PUC-Rio, in partnership with CentraleSupelec EM2C Laboratory. First, isothermal flow simulations have been performed within the swirler and the combustion chamber. Then, using classical premixed combustion models, two distinct flame regimes (14) have been numerically characterized. Comparisons with experimental results have been drawn also.

The isothermal flow results have shed light upon the flow behaviour within the swirler and combustion chamber, as well as the mesh refinement and turbulence model impacts on the numerical solution. The swirl number has three levels of mesh refinements, three turbulence models and wall boundary conditions. The swirl number has been shown to decrease when a finer mesh is used, converging to a value of $S \approx 0.70$. The boundary conditions of slip walls have yielded a significantly higher swirl number, and an over-simplified flow field. The three turbulence models yield similar qualitative results and swirl numbers. The recirculation zones and swirling jet locations have been identified within the combustion chamber. The direct comparison of isothermal and reactive flow results allows to understand the impact of combustion on the flow field structure and turbulence properties: the chemical reaction heat release causes a flow acceleration, which closes the inner recirculation zone and limits its extension. The choice of the most adequate turbulence model is, however, impossible, since flow velocity measurements within the combustion chamber are not available.

The reactive flow results have shown that the obtained flame topologies agree qualitatively with their experimental counterpart. The two-equation, premixed combustion Extended Coherent Flamelet Model, coupled with the realizable $k - \epsilon$ turbulence model was able to predict the average behaviour of flame topologies II and IV, observed experimentally (13), albeit at different equivalence ratio values. The one-equation, Zimont Turbulent Flame Closure model has also been applied, but has led to an over-simplification of the flame

structure, under-predicting the flame surface density.

In light of the obtained results, perspectives for this work include:

- The improvement of the mesh refinement at the swirler, as discussed in section 4.1, which has been shown to impact the calculated swirl number and flow field within this device.
- The implementation of a taller combustion chamber ($H_c = 170$ mm), similar to that experimentally studied, as well as a refined mesh at its upper region. This adjustment is of special interest when a leaner combustion configuration is of interest, such as regime I. It has been observed experimentally that these flames are longer, and they have not been adequately reproduced with the adopted short combustion chamber.
- The investigation of the flame location at the Borghi diagram, discussed at section 4.4. A more rigorous estimate of the flame thickness could change the location of the obtained flames at the diagram significantly. Nevertheless, the implementation of premixed combustion models that are not limited by flame/turbulence interaction assumptions should be considered, such as PDF transport models (58).
- The effect of the implementation of finite wall heat fluxes on the resulting flow field and combustion properties. The high velocity flow of hot gases adjacent to the combustion chamber walls suggests that heat fluxes may not be negligible, which has been seen in experiments conducted elsewhere (59). The assumption of adiabatic walls could be, therefore, improper.
- Full determination of combustion regime diagrams, i.e., as a function of equivalence ratio and volumetric flow rate, thus allowing to categorize the flame regimes stability and boundary limits, in accordance to the experimental studies [Fig. 2.3 (13)].
- The application of Large Eddy Simulations, in order to improve the prediction of the unsteady behaviour and thermoacoustic instabilities, and also predict the coherent turbulent structures.

Bibliography

- [1] BORGNAKKE, C.; SONNTAG, R. E.. **Fundamentals of Thermodynamics**. Wiley, University of Michigan, 8th edition, 2013.
- [2] IPIECA. **Open cycle gas turbines**. IPIECA, 2014. Access in: April 2019.
- [3] LEFEBVRE, A. H.. **The role of fuel preparation in low-emission combustion**. *Journal of Engineering for Gas Turbines and Power*, 117:617–654, 1995.
- [4] ZELDOVICH, Y. B.. **The oxidation of nitrogen in combustion explosions**. *Acta Physicochimica U.S.S.R.*, 21:577–628, 1946.
- [5] HUANG, Y.; YANG, V.. **Dynamics and stability of lean-premixed swirl-stabilized combustion**. *Progress in Energy and Combustion Science*, 35:293–364, 2009.
- [6] LEONARD, G.; STEGMAIER, J.. **Development of an aero-derivative gas turbine dry low emissions combustion system**. *Journal of Engineering for Gas Turbines and Power*, 116:542–546, 1994.
- [7] JOSHI, N. D.; EPSTEIN, M. J.; DURLAK, S.; MARAKOVITS, S.; SABLA, P. E.. **Development of a fuel air premixer for aeroderivative dry low emissions combustors**. ASME Paper, 1994-GT-0253, 1994.
- [8] JOSHI, N. D.; MONGIA, H. C.; LEONARD, G.; STEGMAIER, J. W.; VICKERS, E. C.. **Dry low emissions combustors development**. ASME Paper, 1998-GT-0310, 1998.
- [9] CANDEL, S.; DUROX, D.; SCHULLER, T.; BOURGOUIN, F.; MOECK, J. P.. **Dynamics of swirling flames**. *Annual Review of Fluid Mechanics*, 46:147–173, 2014.
- [10] GOY, C. J.; JAMES, S. R.; REA, S.. **Monitoring combustion instabilities: E.ON UK's experience**. chapter 8. in: Lieuwen T, Yang V, editors. **combustion instabilities in gas turbine engines: operational experience, fundamental mechanisms, and modeling**. *Progress in Astronautics and Aeronautics*, 210:163–175, 2005.

- [11] FIGUEIRA DA SILVA, L. F.; MERGULHÃO, C. S.; PITON, L.; SCOUFLAIRE, P.; DARABIHA, N.. **Experimental study of a lean premixed turbulent swirling flame stabilization**. 24th International Congress of Mechanical Engineering, p. 1–9, 2017.
- [12] PITON, L.; NOBREGA, G. S.; FIGUEIRA DA SILVA, L. F.; SCOUFLAIRE, P.; DARABIHA, N.. **Experimental study of the influence of the swirl number on lean premixes combustion regimes**. 17th Brazilian Congress of Thermal Sciences and Engineering, p. 1–9, 2018.
- [13] NOBREGA, G. S.; PITON, L.; FIGUEIRA DA SILVA, L. F.; SCOUFLAIRE, P.; DARABIHA, N.. **Experimental study of the effect of the swirl number on premixed combustion regimes and flame topologies**. 11th Mediterranean Combustion Symposium, p. 1–12, 2019.
- [14] SHANBHOUE, S. J.; SANUSI, Y. S.; TAAMALLAH, S.; HABIB, M. A.; MOKHEIMER, E. M. A.. **Flame macrostructures, combustion instability and extinction strain scaling in swirl-stabilized premixed CH₄/H₂ combustion**. *Combustion and Flame*, 163:1–14, 2015.
- [15] GUIBERTI, T. F.; DUROX, D.; ZIMMER, L.; SCHULLER, T.. **Analysis of topology transitions of swirl flames interacting with the combustor side wall**. *Combustion and Flame*, 162:1–16, 2015.
- [16] POPE, S. B.. **Turbulent Flows**. University of Cambridge, Edinburgh Building, Cambridge, CB2 2RU, UK, 1st edition, 2000.
- [17] SCOTT BREWSTER, B.; CANNON, S. M.; FARMER, J. R.; MENG, F.. **Modelling of lean premixed combustion in stationary gas turbines**. *Progress in Energy and Combustion Science*, 25:353–385, 1999.
- [18] SMITH, G. P.; GOLDEN, D. M.; FRENKLACH, M.; MORIARTY, N. W.; EITENEER, B.; GOLDBERG, M.; BOWMAN, C. T.; HANSON, R. K.; SONG, S.; GARDINER JR, W. C.; LISSANSKI, V. V.; QIN, Z.. http://www.me.berkeley.edu/gri_mech/. Berkeley Mechanical Engineering, 1999.
- [19] MANSOURI, Z.; AOUISSI, M.; BOUSHAKI, T.. **A numerical study of swirl effects on the flow and flame dynamics in a lean premixed combustor**. *International Journal of Heat and Technology*, 34:227–235, 2016.

- [20] MANSOURI, Z.; BOUSHAKI, T.; AOUISSI, M.; GÖKALP, I.. **Computational investigation of a swirled premixed burner using hybrid RANS-LES method.** *Progress in Energy and Combustion Science*, 35:293–364, 2009.
- [21] ROCHETTE, B.; COLLIN-BASTIANI, F.; GICQUEL, L.; VERMOREL, O.; VEYNANTE, D.. **Influence of chemical schemes, numerical method and dynamic turbulent combustion modeling on led of premixed turbulent flames.** *Combustion and Flame*, 191:1–14, 2018.
- [22] ZETTERVAL, N.; NORDIN-BATES, K.; NILSSON, E. J. K.; FUREBY, C.. **Large eddy simulation of a premixed bluff body stabilized flame using global and skeletal reaction mechanisms.** *Combustion and Flame*, 179:1–22, 2017.
- [23] COLIN, O.; DUCROS, F.; VEYNANTE, D.; POINSOT, T.. **A thickened flame model for large eddy simulations of turbulent premixed combustion.** *Physics of Fluids*, 12:1843–1863, 2000.
- [24] LOURIER, J. M.; STÖHR, M.; NOLL, B.; WERNER, S.; FIOLITAKIS, A.. **Scale adaptive simulation of a thermoacoustic instability in a partially premixed lean swirl combustor.** *Combustion and Flame*, 183:1–15, 2017.
- [25] VOLPIANI, P. S.; SCHMITT, T.; VEYNANTE, D.. **Large eddy simulation of a turbulent swirling premixed flame coupling the TFLES model with a dynamic wrinkling formulation.** *Combustion and Flame*, 180:1–12, 2017.
- [26] KRAUS, C.; SELLE, L.; POINSOT, T.. **Coupling heat transfer and large eddy simulation for combustion instability prediction in a swirl burner.** *Combustion and Flame*, 191:1–13, 2018.
- [27] SCHULZ, O.; DOLL, U.; EBI, D.; DROUJKO, J.; BOURQUARD, C.; NOIRAY, N.. **Thermoacoustic instability in a sequential combustor - large eddy simulation and experiments.** *Proceedings of the Combustion Institute*, 37:1–8, 2018.
- [28] NOH, D.; KARLIS, E.; NAVARRO-MARTINEZ, S.; HARDALUPAS, Y.; TAYLOR, A. M. K. P.; FRIEDRICH, D.. **Azimuthally-driven subharmonic thermoacoustic instabilities in a swirl-stabilised combustor.** *Proceedings of the Combustion Institute*, 37:1–9, 2018.

- [29] HAN, X.; LAERA, D.; MORGANS, A. S.; SUNG, C. J.; HUI, X.; LIN, Y. Z.. **Flame macrostructures and thermoacoustic instabilities in stratified swirling flames**. Proceedings of the Combustion Institute, 37:1–8, 2018.
- [30] CAETANO, N. C.; FIGUEIRA DA SILVA, L. F.. **A comparative experimental study of turbulent non premixed flames stabilized by a bluff-body burner**. Experimental Thermal and Fluid Science, 63:20–33, 2015.
- [31] DUROX, D.; MOECK, J. P.; BOURGOUIN, J-F.; MORENTON, P.; VIAL-LON, M.; SCHULLER, T.; CANDEL, S.. **Flame dynamics of a variable swirl number system and instability control**. Combustion and Flame, 160:1729–1742, 2013.
- [32] MAGISTER CONSORTIUM.. **Magister consortium**. <https://www.utwente.nl/en/et/magister/AboutMagister/Consortium/>, 2019.
- [33] FLUENT INC.. **Standard, RNG, and realizable k- ϵ models theory**. , 2006. Access in: July 2019.
- [34] JONES, W. P.; LAUNDER, B. E.. **The prediction of laminarization with a two-equation model of turbulence**. International Journal of Heat and Mass Transfer, 15:301–314, 1972.
- [35] YAKHOT, V.; ORSZAG, A.. **Renormalization group analysis of turbulence: I. basic theory**. Computers Fluids, 1:1–51, 1986.
- [36] SHIH, T-H.; LIOU, W. W.; SHABIR, A.; YANG, Z.; ZHU, J.. **A new $k-\epsilon$ eddy viscosity model for high reynolds number turbulent flows**. Computers Fluids, 24:227–238, 1995.
- [37] FLUENT INC.. **Standard and SST k- ω models theory**. , 2006. Access in: July 2019.
- [38] WILCOX, D. C.. **Turbulent modelling for CFD**. DCW Industries, Inc., La Canada, California, 2nd edition, 1998.
- [39] MENTER, F. R.. **Two-equation eddy-viscosity turbulence models for engineering applications**. AIAA Journal, 32:1598–1605, 1994.
- [40] PETERS, N.. **Turbulent combustion**. Cambridge University Press. doi:10.1017/CBO9780511612701, The Edinburgh Building, Cambridge CB2 2RU, UK, 1st edition, 2000.

- [41] ZIMONT, V.; POLIFKE, W.; WEISENSTEIN, W.. **An efficient computational model for premixed turbulent combustion at high reynolds numbers based on a turbulent flame speed closure.** Journal of Engineering for Gas Turbines and Power, 120:526–532, 1998.
- [42] BLINT. **Principles of Combustion.** Wiley-Interscience, New-York, 1st edition, 1988.
- [43] ANSYS, INC.. **Extended coherent flamelet model theory.** , 2009. Access in: July 2019.
- [44] ZIMONT, V. L.. **Gas premixed combustion at high turbulence. turbulent flame closure combustion model.** Experimental Thermal and Fluid Science, 21:179–186, 2000.
- [45] BRAY, K. N. C.; LIBBY, P. A.; MOSS, J. B.. **Unified modeling approach for premixed turbulent combustion — part I: General formulation.** Combustion and Flame, 61:87–102, 1985.
- [46] DARABIHA, N.; GIOVANGIGLI, V.; TROUVÉ, A.; CANDEL, S. M.; ESPOSITO, E.. **Coherent flame description of turbulent premixed ducted flames.** Turbulent Reactive Flows, 40:591–637, 1989.
- [47] BORGHI, R.; CHAMPION, M.. **Modélisation et théorie des flammes.** Editions TECHNIP, 1st edition, 2000.
- [48] ZIMONT, V. L.. **Theory of turbulent combustion of a homogeneous fuel mixture at high reynolds numbers.** Combustion Explosion and Shock Waves, 15:305–311, 1979.
- [49] ZIMONT, V. L.; LIPATNIKOV. **A numerical model of premixed turbulent combustion of gases.** Chemical Physics Reports, 14:993–1025, 1995.
- [50] POINSOT, T.; VEYNANTE, D.. **Theoretical and Numerical Combustion.** R. T. Edwards Inc., Philadelphia, PA 19118 USA, 2nd edition, 2005.
- [51] CANDEL, S. M.; POINSOT, T. J.. **Flame stretch and the balance equation for the flame area.** Combustion Science and Technology, 70:1–15, 1990.
- [52] MENEVEAU, C.; POINSOT, T.. **Stretching and quenching of flamelets in premixed turbulent combustion.** Combustion and Flame, 86:311–332, 1991.

- [53] COPPENS, F. H. V.; DE RUYCK, J.; KONNOV, A. A.. **Effect of hydrogen enrichment on adiabatic burning velocity and NO formation in methane + air flames**. *Experimental Thermal and Fluid Science*, 31:437–444, 2007.
- [54] SMITH, G. P.; GOLDEN, D. M.; FRENKLACH, M.; MORIARTY, N. W.; EITENEER, B.; GOLDENBERG, M.; BOWMAN, C. T.; HANSON, R. K.; SONG, S.; GARDINER JR, W. C.; LISSIANSKI, V. V.; QIN, Z.. **Grimech 3.0**. http://www.me.berkeley.edu/gri_mech/, 1999. Access in: April 2019.
- [55] WANG, Y.; YANG, V.. **Central recirculation zones and instability waves in internal swirling flows with an annular entry**. *Physics of Fluids*, 30:1–20, 2018.
- [56] SPALDING, D. B.. **A single formula for the law of the wall**. *Applied Mechanics*, 28(3):455–458, 1961.
- [57] GROSSEUVRES, R.; COMANDINI, A.; BENTAIB, A.; CHAUMEIX, N.. **Combustion properties of H₂/N₂/O₂/steam mixtures**. *Proceedings of the Combustion Institute*, 37:1537–1546, 2019.
- [58] FOX, R. O.. **Computational models for turbulent reacting flows**. Cambridge University Press, The Edinburgh Building, Cambridge CB2 2RU, UK, 1st edition, 2003.
- [59] GUIBERTI, T.F.; DUROX, D.; SCOUFLAIRE, P.; SCHULLER, T.. **Impact of heat loss and hydrogen enrichment on the shape of confined swirling flames**. *Proceedings of the Combustion Institute*, 35:1385–1392, 2015.